Investigation of lepidolite surface properties: Insights from solid-gas and solid-liquid interfaces analyses

Chloé Korbel, J.P. Pinheiro, Benedicte Prelot, Angelina Razafitianamaharavo, F. Villieras, Oscar Alberto Gamba Vasquez, Y. Foucaud

Investigation of lepidolite surface properties: insights from solid-gas and solid-liquid interfaces analyses

C. Korbel[1*], J.P. Pinheiro[2], B. Prelot[3], A. Razafitianamaharavo[2], F. Villieras[2], O.Gamba[1], Y. Foucaud[1*]

[1] Université de Lorraine, CNRS, GeoRessources, F-54000, Nancy France

[2] Université de Lorraine, CNRS, LIEC, UMR 7360 CNRS, 15 avenue du Charmois, 54500 Vandoeuvre-les-Nancy, France

[3] Institut Charles Gerhardt Montpellier, UMR 5253 CNRS-UM2, Agrégats, Interfaces et Matériaux pour l'Energie, CC 1502, Pl Eugene Bataillon, F-34095 Montpellier 5, France

*Corresponding authors: chloe.korbel@univ-lorraine.fr ; yann.foucaud@univ-lorraine.fr

Highlights

- In-depth characterization of surface properties of lepidolite was conducted;
- Colloidal and surface properties are different since IEP = 2.5 and PZC = 8.5;
- Derivative of the pH-titration curve exhibited 3 surface pKa at 4.8, 6.2, and 7.8;
- These pKas were attributed to aluminol and silanol surface adsorption sites;
- This will have a strong impact for the beneficiation of lepidolite by flotation.

Abstract

This study proposes an in-depth exploration of the surface properties of lepidolite, a lithium-bearing phyllosilicate mineral, using nitrogen and argon adsorption isotherms, electrophoretic mobility measurements, and surface titration experiments. The solid-gas and solid-liquide interfaces analyses allow characterizing the surface heterogeneity of lepidolite, highlighting the dominance (~ 80%) of the basal surfaces over the lateral surfaces (~ 20%) in the total specific surface area. The N_2 adsorption isotherm exhibited various adsorption sites, including the exposed interfoliar cations and the empty hexagonal cavities related to the cleavage process, on the basal planes, or the exposed oxygen and fluorine atoms on the lateral surfaces. Besides, the solid-liquid interfaces analyses highlighted a significant difference between the isoelectric point and point of zero charge of lepidolite, with pH values of 2-3 and 8.5-9, respectively, which demonstrated the importance of monitoring surface observables such as the surface potential

rather than the zeta potential. Noteworthily, surface titration experiments allowed to identify distinct surface sites with specific pKa values that were discussed and demonstrated that the potassium interfoliar cations are exchanged with protons when the pH is decreased. These findings allow to gain understanding in the lepidolite's surface properties and will provide valuable implications for lithium extraction by the froth flotation method, a mineral beneficiation process based on the surface properties of minerals. Also, this research will pave the road in the in-depth investigation of physicochemical properties of surfaces in order to finely tune the metal extraction in the current energy transition context.

1. Introduction

The in-depth exploration of solid-gas and solid-liquid interfaces is paramount in numerous pivotal industrial applications. These domains encompass electronics, adsorption for gas purification or separation, heterogeneous catalysis, the agri-food and pharmaceutical sectors, as well as environmental depollution and metal extraction (Buckton, 2000; Krog et al., 1989; Lu and Bitsianes, 1968; Richardson, 1982). Considering the growing demand for metals, particularly related to the ongoing energy transition, metal extraction is facing emerging challenges related to the decrease of the metal grades and to the increasing complexity of mineral deposits, in which the target minerals are more and more finely disseminated (Farrokhpay et al., 2021; Roy, 2009; Upadhyay and Venkatesh, 2006). In this context, the froth flotation separation method has become widely employed for the extraction of metals from ores and this technique is nowadays used to process more than 2 billion tons of ores every year. Froth flotation is based on the selective adsorption of reagents on powdered minerals surfaces to finely tune their wettability (Faris et al., 2017), selectively making the target mineral(s) surfaces hydrophobic. After the reagents adsorption, air bubbles are added in flotation cells to recover hydrophobic particles in a froth phase, whereas the hydrophillic particles are recovered from the suspension. Hence, froth flotation is very sensitive upon the mechanisms acting at the mineral-water and mineral-gas interfaces of powdered minerals.

Over the past decade, froth flotation has started facing significant hurdles as the intricacy of metallic deposits has significantly increased (Gorain, 2013). This complexity raises challenges in the objective of attaining a selective adsorption of surfactants onto the desired metal-bearing minerals. Recently, the flotation of lithium-bearing minerals has become a significant topic of concern (Li et al., 2019), due to the exponential industrial demand for lithium to build Li-ion batteries for electric vehicles. Among the lithium-bearing minerals, lepidolite $[K(Li,Al)_3(Si,Al)_4O_{10}(F,OH)_2$ stands out as the primary source of lithium from hard rock deposits in Europe (Christmann et al., 2015; Gourcerol et al., 2019; Kesler et al., 2012). The beneficiation of lepidolite-bearing ores therefore mainly depends upon the selective flotation of this phyllosilicate mineral from quartz and feldspar, which still represents a technical and scientific challenge (Korbel et al., 2023; Sahoo et al., 2022; Tadesse et al., 2019). Hence, to successfully optimize the selectivity and the performances of the lepidolite flotation, the selectivity of adsorption of flotation reagents has to be finely tuned. For that, acquiring a thorough understanding of interfaces between lepidolite and water and air is of paramount importance.

Mineral surfaces, and therefore interfaces, are known to present a significant heterogeneity, which is related to the different types of crystallographic they exhibit (Villieras et al., 2002). Moreover, each type of exposed crystallographic plane exhibits an energy heterogeneity between the reactive surface sites, originating from the nature of minerals that are assemblies of anions and cations (Gao et al., 2014; Moon and Fuerstenau, 2003). Therefore, methods for analysing the heterogeneity of surfaces, specifically adapted for the study of anisotropic materials such as phyllosilicates, have been developed over the past decades, using high-resolution adsorption isotherms (Villieras et al., 1997) or surface titration (Mbey et al., 2019; Prelot, 2001). Besides, surface-specific analytical methods such as X-ray photoelectron spectroscopy (Deng and Ou, 2024; Watts and Wolstenholme, 2019; Xu et al., 2024; Xue et al., 2024), small-angle X-ray scattering (Pernyeszi and Dékány, 2003), atomic force microscopy (Xing et al., 2018), or Fourier Transform Infrared (FTIR) spectroscopy (Antti and Forssberg, 1989) can also be used to gain understanding in the physicochemical phenomena acting on the surface (Brus et al., 2004;

Massaro et al., 2002; Ratner and Castner, 2020). Recently, Foucaud and co-workers highlighted the possibility to use non-linear optic methods to specifically monitor surface reactions by understanding the origin of the surface-specific signal (Foucaud et al., 2021). In addition, interesting insights are now being provided by the growing use of molecular modelling methods, based either on force fields or on first principles (Churakov et al., 2015; Dell'Angelo et al., 2024), particularly for unravelling the adsorption mechanisms involved in flotation processes (Foucaud et al., 2019). These methods allow acquiring a thorough understanding of the influence of the heterogeneity of the mineral surfaces on adsorption mechanisms since they explicitely consider the ions in the bulk crystal phase, in the bulk liquid phase, and on the surfaces (Foucaud et al., 2018). However, these methods still have limitations when considering solid-liquid interface since the surface state cannot be described (surface speciation, pH value, etc.).

However, very few investigations on surface properties of lepidolite, experimental or theoretical, have been undertaken to the best of our knowledge. Moreover, theoretical chemistry methods require an extensive knowledge of the surface heterogeneity and surface speciation to be efficiently and accurately conducted (Fukushi and Sverjensky, 2007). This work aims to deepen our understanding of lepidolite's surface properties, including their heterogeneity and their speciation, to optimize the selective adsorption of surfactants onto its surface and to serve as basis for molecular modelling methods. For that, we use an original combination of gas adsorption experiments, electrophoretic mobility measurements, and potentiometric surface titrations. This work will not only propose an original combination of experimental methods for investigating minerals surface properties, but gives insights for the development of innovative, more efficient, and environment-friendly routes to beneficiate this Li-bearing mineral in the current energy transition context.

2. Materials and Methods

2.1. Sample

The lepidolite mineral used for this study comes from a brasilian ore and was purchased from Minerama (France). It was powdered using a tungsten planetary mill to produce a sample fine enough (0-20 µm) for X-ray diffraction analysis, gas adsorption, and surface titration. A finer sample (< 10 µm) was produced for electrophoretic mobility experiments, to prevent the sample from sedimentation during assays.

X-ray diffraction (XRD) analysis

The measurement was carried out using a back-loaded sample holder to limit the overexpression of the (001) lepidolite crystallographic planes, which is a point commonly discussed for the analysis of phyllosilicate minerals (Kleeberg et al., 2008; Silva et al., 2011). The X-ray diffraction (XRD) pattern of lepidolite was acquired at room temperature. The measurement was performed using a D2 Phaser diffractometer (Bruker, Germany) equipped with a LYNXEYE detector and operating at 30 kV and 10 mA. The X-ray source was a the Kα radiation of a copper anode (1.5406 Å).

ICP-OES

ICP-OES assays were carried out using a 7400 Duo spectrometer (Thermo Fisher Scientific, USA). Wavelengths used for Al_2O_3, CaO, Fe_2O_3, K_2O, MgO, MnO, NaO, P_2O_5, Rb, SiO_2, and W quantifications were 396.152, 315.887, 259.940, 766, 279, 257, 818.326, 178.284, 780.023, 251.611 and 207.911 nm, respectively. Reliability of the chemical assays was assessed using a standard sample, with a mineralogical and chemical composition close to that of our sample, provided by SARM (CRPG, France). This standard sample was analysed using the same instrument. Before acquisition, the sample was leached using lithium metaborate, which is a common method for silicate leaching process (Pinto et al., 2012; Ramsey et al., 1995). Therefore, the direct quantification of lithium could not be achieved using this method.

2.2. Gas adsorption isotherms

2.2.1. Specific surface area determination

Gas adsorption measurements were performed on a Belsorp max II adsorbometer (Microtrac MRB, Germany), with an initial mass of lepidolite of 1.17 g. The lepidolite sample was outgassed at 393.15 K overnight to allow removal of impurities such as vapor water prior to measurement (mass loss estimated at approximately 3.5%). High purity nitrogen (> 99.9995%), provided by Alphagaz (France), was used as the probe of the adsorption experiment. The adsorption isotherm was acquired at 77 K. The specific surface area was determined using the BET method and the pore volume was calculated using de Boer (or t-plot) method (Brunauer et al., 1938; De Boer et al., 1966; Hudec et al., 2002; Salvador et al., 2002).

2.2.1. Low-pressure argon and nitrogen adsorption at 77 K

Low-pressure adsorption isotherms were used to deeply investigate the surface heterogeneity of lepidolite. Such a method is particularly suitable for studying surface heterogeneity of phyllosilicates (Michot et al., 1994; Villieras et al., 1992). The experimental procedure consists of recording high-resolution adsorption isotherms on a lab-built automatic quasi-equilibrium volumetric setup described elsewhere (Bardot, 1998; Michot et al., 1990; Villieras et al., 1992). The quasi-equilibrium technique is based on the adsorbate introduction with a slow, constant, and continuous flow rate through a micro leak. High-resolution adsorption isotherms were acquired at least up to the BET domain, corresponding to the formation of the first adsorbed layer. All these experiments were carried out at 77 K.

The high purity argon and nitrogen used here were provided by Alphagaz (France). The lepidolite sample was outgassed overnight at 393.15 K, to remove impurities such as adsorbed water from the mineral surface, under a residual pressure of 10^{-4} Pa. The procedure for the acquisition using this experimental setup is thoroughly described by Villieras and co-authors (Villieras et al., 1992). This method allows obtaining a large number of experimental data points on the adsorption isotherms. Hence, the derivative of the experimental adsorption isotherms can be calculated as a function of the logarithm of relative pressure, $\ln(P/P_0)$, which corresponds to the adsorption energy expressed in kT or RT units. The obtained derivative adsorption isotherm can then be

158 considered as a fingerprint of the adsorption energy distribution for the considered gaseous probe
159 (here, either argon or nitrogen).

160 The total derivative adsorption isotherm on a heterogeneous surface can be simulated by using
161 concepts describing adsorption phenomena on heterogeneous surfaces and following the
162 Derivative Isotherm Summation (DIS) procedure (Villieras et al., 1992; Villieras et al., 1997):

$$\theta_t = \sum_{i=1}^{n} X_i \theta_{it} \,, \qquad with\ \theta_{it} = \int_{\Omega} \theta_i(\varepsilon)\chi_i(\varepsilon)d\varepsilon \tag{1}$$

163 where θ_t is the total adsorption isotherm, θ_{it} is the adsorption isotherms on the different faces of
164 the particle, X_i is its contribution to θ_t, ε is the adsorption energy, Ω is the physical domain of ε,
165 $\theta_i(\varepsilon)$ is a local theoretical adsorption isotherm, and $\chi_i(\varepsilon)$ is the dispersion of ε on the *ith* face or
166 adsorption domain.

167 Using this method, the total derivative adsorption isotherm is considered as the sum of local
168 theoretical adsorption isotherms, with or without lateral interactions (*i.e.*, Langmuir,
169 Bragg_Williams-Temkin, BET, HILL, Dubinin–Astakhov, etc.). In the present case, the BET-derived
170 formalism was used as the local θ_{it} isotherms in Eq.1 with the Hill formalism to consider possible
171 lateral interactions between adsorbed molecules. All the DIS were computed using the
172 condensation adsorption energy distribution (CAED) method in order to calculate local isotherms
173 contributing to the first monolayer (Charmas et al., 2002).

174 **2.3. Atomic Force Microscopy (AFM) Imaging**

175 AFM experiments were performed with a FastScan Dimension Icon with Nanoscope V controller
176 (Bruker, Germany). AFM imaging was carried out in air Peak Force Tapping mode at ambient
177 temperature. Sharp triangular silicon nitride tips (NPG-10, Bruker AFM probes) were used with
178 nominal values of the spring constant and curvature radius around 0.32 ± 0.2 $N \cdot m^{-1}$ and 30 nm
179 respectively. A lepidolite suspension with few particles was prepared in high purity Milli-Q water
180 at pH 9 and was sonicated for 5 min. A drop of this suspension was deposited on a borosilicate

glass slide and then immediately dried at ambient temperature before the measurements with AFM.

2.4. Electrophoretic mobility measurements

The electrophoretic mobility was measured using a ZetaCompact zetameter (CAD intruments, France). A background electrolyte was used to maintain the ionic strength constant between the various measurements. The background electrolyte was prepared using KCl salt with purity above 99.0% (Sigma Aldrich, Germany) and ultrapure water type II, resistivity of 18.2 MΩ·cm (Aquadem, Veolia, France). For acquisitions, KCl was used as the background electrolyte. KCl with a concentration of 0.1 mol·L^{-1} was prepared so that the ionic strength was considered constant over a wide range of pH, *i.e.*, from pH 2 to 12 (Cases, 1967). The measurements were all conducted using this ionic strength since lepidolite is supposed to have an iso-electric point (IEP) at strong acidic pH values, *i.e.*, below a pH value of 3 (Choi et al., 2012; Filippov et al., 2022; Wei et al., 2021).

A suspension was prepared using fine grained lepidolite (< 10 µm) so that no sedimentation occurred during the experiments. For each pH value, a new suspension was prepared, and the desired pH value was attained by adding HCl or KOH. The concentration of base or acid used was adapted to the desired pH value so that the amount of pH modifier added in the solution was neglectable. Then, the suspension was equilibrated for 15 minutes with a magnetic stirrer, and the electrophoretic mobility was measured three times on at least 100 particles for each measurement. After the acquisition, the measurement cell was cleaned with deionised water using a volume equivalent to more than twice the volume of the cell.

2.5. Potentiometric surface titration

2.5.1. Reagents

Titripur® HNO_3 (0.1 mol·L^{-1}) and KOH (0.1 mol·L^{-1}) were provided by SigmaAldrich (Germany) and were of analytical grade. NaOH (0.1 mol·L^{-1}) was purchased from Carl Roth (Germany) and was of analytical grade. KNO_3 and $NaNO_3$ salts were purchased from Sigma Aldrich (Germany) and

were of analytical grade. All the solutions were prepared with Milli-Q water (18.2 MΩ·cm, purelab flex elga). A solution with the adequate ionic strength and pH was prepared for each experiment. The pH calibration was done using five standard solutions, at pH = 4 (pH = 4 (293.15 K): ROTI CALIPURE, Carl Roth, Germany), pH = 5 (pH = 5 (298.15 K): Reagecon, Shannon, Ireland), pH = 7 (pH = 7 (293.15 K): ROTI CALIPURE, Carl Roth, Germany), pH = 9 (pH = 9 (298.15 K): Reagecon, Shannon, Ireland), and pH = 10 (pH = 10 (293.15 K): ROTI CALIPURE, Carl Roth, Germany). Agon (Ar) was used as an inert atmosphere and was provided by Alphagaz (200 bar at 288.15 K, Alphagaz 1 Argon Smartop, compressed Argon, n°UN: 1006, N°CE: 231-147-0).

2.5.2. Material

Titration experiments were carried out using a Titrando 809 (Metrohm, Swiss) linked to 3 auto-burettes Dosino 800 (Metrohm, Swiss). All the tests were programmed and acquired using the Tiamo 2.4. software (Metrohm, Swiss). The suspension was placed in a titration cell cooled by an ecoline staredition RE107 thermostat (Lauda, Germany) equipped with a E100 (Thermometer). Temperature for the titration was set at 298.15 K (± 0.1 K). The suspension was mixed using a PTFE magnetic stirrer. The potential and temperature were recorded using two probes. First, an Orion, ROSS Ultra pH/ATC Triode pH probe (Thermo scientific, USA) was used for the potential. This probe was chosen to prevent degradation of the electrode because of the silicate suspension and was calibrated before and after each test. The second probe, which was used to follow temperature during titration experiments, was a Pt 1000 thermometer probe (Methrom, Swiss). Errors linked to the potential measurement were kept below 5%, as described in the procedure of Szekeres & Tombácz (2012). A CDM210 MeterLab conductometer (Radiometer analytical, France) equipped with a Radiometer analytical probe was used to prepare solutions (blank and suspension) with the same conductivity. The mass of lepidolite introduced in the suspension was measured using a 0.0001 g precision scale (N°249, ML204/01, Mettler Toledo, Swiss).

2.5.3. Procedure

To obtain one titration curve, two tests were carried out: first, a blank using the solution prepared at the adequate pH and ionic strength, and, second, a test with a suspension of 50 mL composed of 25 mg to 50 mg of lepidolite. Ar was continuously bubbling in the suspension before and during the tests to prevent the solution from carbonation, which is known to produce parasite reactions.

2.5.4. High resolution hydroxide adsorption isotherm

In these experiments, 50 mg of lepidolite was titrated in 50 mL of 1 x 10^{-1} mol·L^{-1} KNO_3. Before acquisition, the suspension was equilibrated for 1 hour. Then, acid was added to the suspension until the target pH value was obtained, followed by a second time of equilibration, so that the new suspension was equilibrated while minimizing the amount of reagent added. After equilibration of the suspension, the titration started by adding successive amounts of base between 2 and 10 µL, to obtain a high density of experimental points, until the titration endpoint at pH 10.5 was reached. After each base addition, there was a minimum waiting time of 60 s and a maximum waiting time of 600 s. However, if, after 60 s, a drift criterion of 0.2 mV·min^{-1} was observed, another base addition was immediately done. After the titration, a blank experiment (in absence of lepidolite) was acquired, applying the same experimental procedure.

2.5.5. Modelling

Titration Derivative Isotherm Summation modelling

Titration Derivative Isotherm Summation (TDIS) modelling was carried out using the surface charge calculated with the same method as the one used for the point of zero charge (PZC) determinations. A smoothed derivative from the experimental surface charge was computed, using a MATLAB (*MathWorks, Natick, MA, USA*) cubic spline algorithm with smoothing degrees of 95 or 99%. Then, either the smoothed or experimental data were used for deconvolution in several theoretical local isotherms, according to the TDIS procedure developed by Prelot and co-workers (Prelot, 2001; Prélot et al., 2002). The deconvolution was done using both Langmuir and

BET theoretical isotherms with or without lateral interactions. Parameter optimization was carried out using the PEST (Model-Independent Parameter Estimation and Uncertainty Analysis) optimization software (Doherty, 2015). Further information on the comparison of the previous deconvolution method and the one developed here can be found in supplementary material.

3. Results and Discussions

3.1. Mineralogical and chemical characterisation of the lepidolite sample

The obtained XRD pattern (Figure S9) exhibits peaks of a 2M2 polytype lepidolite, which corresponds to a common natural lepidolite (Korbel et al., 2023). The presence of some common diffraction peaks of albite could highlight the presence of this mineral in the lepidolite sample, although the quantification is difficult using XRD. From Table 1, it seems that no significant contamination of the sample can be observed. The calcium content is low, along with the phosphorus grade, which indicates no contamination by either apatite, fluorite, or calcite. Magnesium is also encountered in very low concentration in the sample, indicating no contamination by any magnesium-bearing mineral, particularly biotite, and no substitution in the octahedral sites of lepidolite crystals. In addition, the sodium content is of about 0.4% and can be related either to a possible substitution of potassium with sodium in the interfoliar site of lepidolite or to the presence of albite in the sample. If the assumption is made that all the sodium is in albite, considering the sodium content of pure albite (11.2% Na_2O), the maximum grade in albite of the sample is 3.6%. The lithium content is assayed at 4.52 %Li_2O, which is consistent with a 2M2 polytype (Levinson, 1953).

Table 1 : Chemical composition of the pure lepidolite sample used in this work.

Element grade (%)												
Al_2O_3	CaO	Fe_2O_3	K_2O	MgO	MnO	Na_2O	P_2O_5	Rb	SiO_2	Li_2O	F	Total
24.37	0.13	0.21	9.74	0.02	0.86	0.40	0.04	0.58	53.40	4.52	6.27	100.54

Besides, small amounts of iron, rubidium, and manganese are found in the sample used in this work, which is common for lepidolite and do not affect the degree of purity of the mineral. From

these assays, the chemical formula can be computed according to the method of Tischendorf et al. (Tischendorf et al., 1999, 1997). Hence the computed formula is given in Equation 2 on the basis of 24 (O, OH, F) and 8 tetrahedral sites.

$$K_{1.67}(Si_{7.16}Al^{IV}_{0.84})(Li_{2.44}Al^{VI}_{3.01})O_{20}(F_{2.66}OH_{0.04}) \quad (2)$$

From this structural formula, in the tetrahedral site, Si fills 89% of the available sites, Al^{IV} filling the remaining ones, wheras in the octahedral sites, Li and Al^{VI} have almost the same abundance in the available sites.

3.2. Insights from solid-gas interface

Porosity and specific surface area determination

The nitrogen adsorption isotherm acquired using a step-by-step method is presented in Figure 1a. The profile of the adsorption-desorption isotherm is characteristic of a mesoporous material with open interparticle porosity (Prelot, 2001; Sing, 1985). The BET specific surface area of this lepidolite sample is estimated to be 21.7 ± 0.9 $m^2 \cdot g^{-1}$. The specific surface area of lepidolite is of the same order of magnitude than the specific surface area data encountered in the literature for muscovite, a phyllosilicate very similar to lepidolite (Papirer et al., 1990, 1986). This measurement demonstrates the specific character of phyllosilicates, which generally exhibit a higher specific surface area than most other silicates (commonly below 1 $m^2 \cdot g^{-1}$) at similar grain size (Brantley and Mellott, 2000; Mukhopadhyay and Walther, 2001).

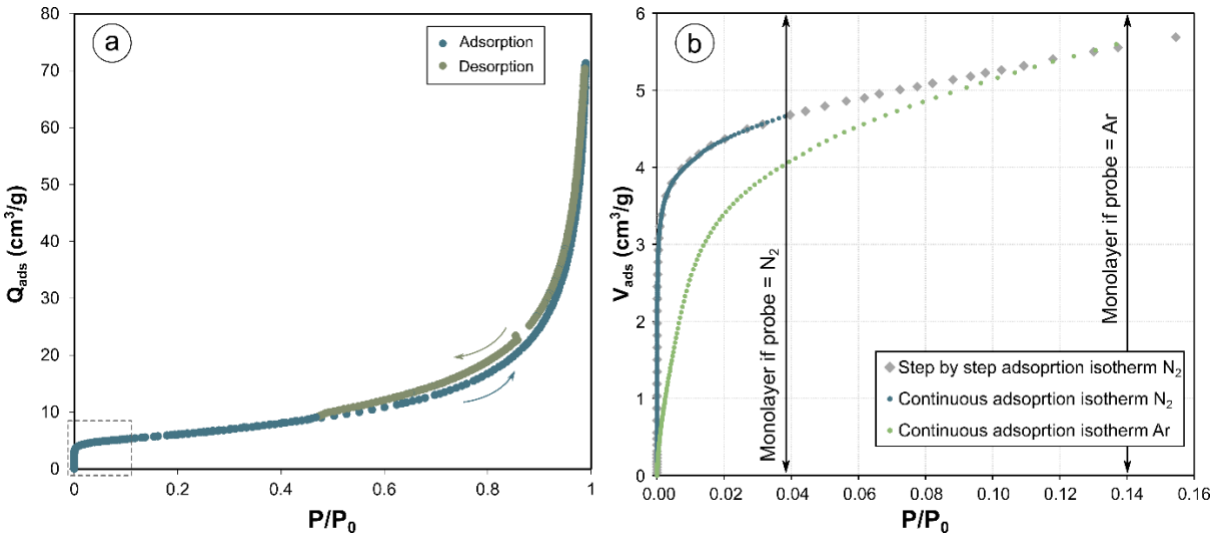

Figure 1: (a) Lepidolite azote adsorption and desorption isotherms at 77K. (b) Zoomed area of Ar and N_2 adsorption isotherms on the lepidolite sample at 77 K.

The *t*-plot method allows estimating a microporous surface area of 3.8 $m^2 \cdot g^{-1}$, corresponding to approximately 6.10^{-3} $cm^3 \cdot g^{-1}$ in liquid volume of nitrogen. The experimental error related to the adsorption experiment can be up to 4%, as highlighted by Perronnet and co-authors (Perronnet et al., 2007). Based on this measurement and on the experimental error, the surface area allocated to micropores is ranging from 3.65 to 3.95 $m^2 \cdot g^{-1}$, which represents 16% to 18% of the total specific surface area of the lepidolite sample. Similar observations were done by the same authors on a smectite sample, for which about 20% of the total surface area was attributed to microporosity (Perronnet et al., 2007). By definition, micropores are assumed to represent all pores which diameter is comprised between 0 and 20 Å (Gregg et al., 1967; Storck et al., 1998). On overall, although this microporosity is difficult to relate to textural or crystallographic features, it could be attributed to (1) the 2-Å-diameter holes formed by the empty hexagonal cavities on the basal surface, to (2) the lateral surfaces that usually represent 10-20% of the total specific surface area, or to (3) steps on the basal surfaces, which are commonly observed for phyllosilicates.

Argon derivative adsorption isotherm

The quasi-equilibrium argon adsorption isotherm of the lepidolite sample is displayed on Figure 1b along with its derivative, presented in Figure 2. The DIS modelling parameters of the experimental derivative are summarised in Table 2. Five local adsorption domains are required to obtain a consistent fit of the experimental values for the lepidolite sample studied in this work.

316 The five local isotherms determined are located at values of ln(P/P_0) of -8.59, -5.98, -4.89, -3.94,
317 and -2.42, respectively (Table 2, Figure 2). The derivative of the argon adsorption isotherm
318 presents a general trend that is very similar to other phyllosilicates: the curve displays a
319 significant peak at intermediate energy values [ln(P/P_0) = -4.89], which is attributed to the
320 adsorption of Ar on the basal faces (Domain 3 in Figure 2) (Cases et al., 2000). This peak is
321 particularly typical of a basal surface of a phyllosilicate with potassium cations exposed on the
322 surface, as previously demonstrated for illite, muscovite and biotite (Sayed Hassan et al., 2006;
323 Villiéras et al., 1997), which is consistent with the fact that potassium cations are exposed on the
324 lepidolite surface. In the aforementioned study, the authors highlighted that the location of this
325 peak is significantly affected by the type of interfoliar cation (*i.e.*, K, Na, Mg, etc.) exposed on the
326 surface of the phyllosilicate (Bardot, 1998). This result is expected, since all these minerals are
327 mainly composed of Si-O-Si hexagonal rings filled with a potassium interfoliar cation. Hence, even
328 considering various minerals, it appears consistent that the adsorption energy of argon on the
329 potassium cation is observed at similar ln(P/P_0) values. Hence, this confirms that the potassium
330 interlayer-compensating cations are exposed on the basal surfaces during the breakage process
331 of lepidolite. Also, this allows firmly concluding that this peak corresponds to the adsorption of Ar
332 molecules on the potassium cations exposed on the lepidolite surface.

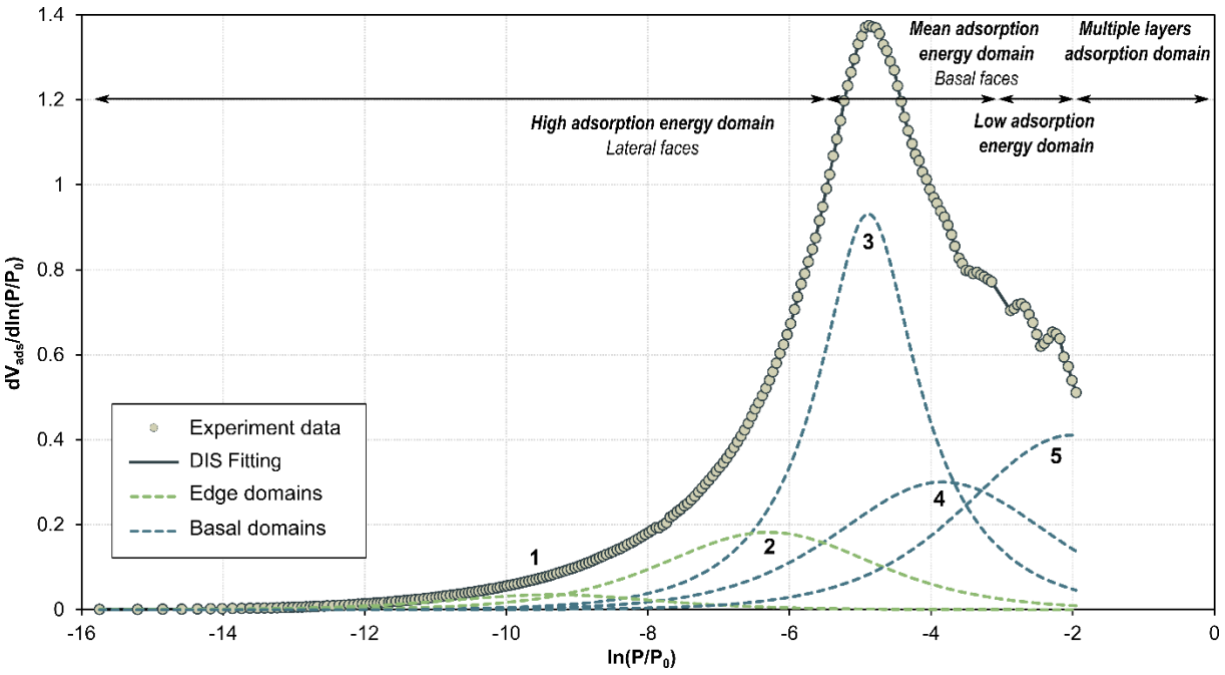

Figure 2 First derivative of the argon adsorption isotherm at 77 K on lepidolite sample and decomposition using the DIS method. The different domains are identified with black numbers.

Along with this main peak, two others peaks located at low energies, *i.e.*, at $\ln(P/P_0)$ = -3.94 and at $\ln(P/P_0)$ = -2.42, respectively, can be observed. These two peaks are also commonly observed for phyllosilicates and are generally also attributed to basal surfaces (Michot et al., 1994). Considering the low surface (1.3 $m^2 \cdot g^{-1}$) represented by the Domain 4, the corresponding peak, located at $\ln(P/P_0)$ = -3.94, could be attributed to steps on the basal surfaces, which is a common morphological feature observed for phyllosilicates. Meanwhile, the peak corresponding to Domain 5, located at $\ln(P/P_0)$ = -2.42, presents a surface very similar to the peak attributed to Domain 3 (7.8 $m^2 \cdot g^{-1}$ and 7.7 $m^2 \cdot g^{-1}$, respectively). Assuming that, during the cleavage process, half of the interfoliar potassium cations go on each of the two created surfaces, half of the hexagonal cavities on the basal surfaces are occupied by a potassium cation while half of the hexagonal cavities are empty, as suggested by Elmi and co-workers using X-ray photoelectron spectroscopy on lepidolite crystals (Elmi et al., 2014). Based on the similar surfaces represented by Domains 3 and 5, the peak corresponding to Domain 5 could therefore be attributed to the adsorption of Ar molecules on empty hexagonal cavities on the basal surfaces of lepidolite, which number is equivalent to the number of potassium cations.

Finally, the derivative experimental isotherm also presents two broad peaks at higher energies, *i.e.*, for the lowest values of $\ln(P/P_0)$ (Figure 2). These two local high-energy adsorption isotherms, located at $\ln(P/P_0)$ = -5.98 and $\ln(P/P_0)$ = -8.58, respectively, can be attributed to the adsorption of Ar molecules on the lateral surfaces of lepidolite, considering their high energy (Bardot, 1998; Michot et al., 1994). These peaks could correspond either to the Al and Li cations exposed on the lateral surfaces, resulting in two different peaks, or to the F^-, OH^- or O^{2-} anions exposed on the lateral surfaces, also resulting in two different peaks. The 3:1 ratio between Domain 2 and Domain 1 in terms of specific surface area is in agreement with the distribution of these cations and anions exposed in the octaedra.

Table 2: Parameters obtained by the DIS simulation for the Ar adsorption derivative isotherm, surface area per domain (in absolute value and in percentage of the total specific surface area), and attribution of the different peaks to types of surfaces and to surface adsorption sites.

	Domain 1	Domain 2	Domain 3	Domain 4	Domain 5
$\ln(P/P_0)$	-8.58	-5.98	-4.89	-3.94	-2.42
ω/kT	-0.3	0.7	1.9	2	0.1
Surface ($m^2 \cdot g^{-1}$)	1.0	3.0	7.7	1.3	7.8
Surface (%)	4.8	14.4	37.0	6.3	37.5
Attribution hypothesis	Octahedral cations	Octahedral anions	Potassium cations	Steps	Empty hex. cavities
Type of surface	Lateral	Lateral	Basal	Basal	Basal

Considering the bulk area of the argon molecule and knowing the adsorbed Ar volume, the specific surface area of each type of surface (basal and lateral) of lepidolite can be calculated based on Table 2. Since Domains 1 and 2 correspond to lateral surfaces and Domains 3, 4, and 5 correspond to basal surfaces, the contributions of each type of surface are $S_{lateral}$ = 4.0 $m^2 \cdot g^{-1}$ and S_{basal} = 16.7 $m^2 \cdot g^{-1}$. Hence, the specific surface area originating from the basal planes (81% of the total specific surface area) is largely dominant over the contribution of the lateral planes (19% of the total specific surface area). This result provides crucial insights for the study of the adsorption

of flotation reagents on lepidolite: the lateral surfaces do not represent enough surface to adsorb the reagents and, therefore, these latter probably adsorb on low-energy domains originating from the basal surfaces. From these calculations, an average morphology of the lepidolite particles can be estimated using a squared plate, from the methodology described in Sayed Hassan et al. (2006).

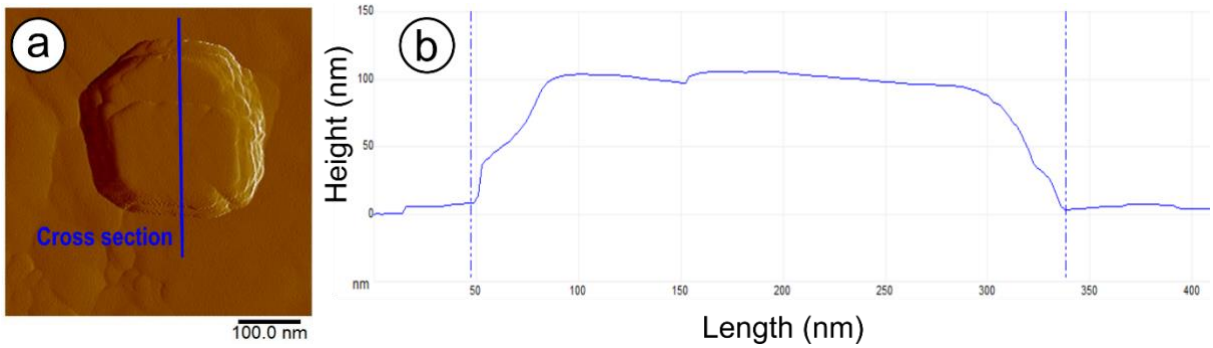

Figure 3: (a) AFM profile on a lepidolite crystal along with (b) a cross section measurement.

Such result can be compared to AFM profile measurements conducted on the same lepidolite crystals used for gas adsorption experiments. One example of AFM acquisition is displayed in Figure 3, which presents the AFM profile of one lepidolite crystal (Figure 3a) along with one cross section measurement performed on the crystal (Figure 3b). The profile displayed in Figure 3a shows that lepidolite has a typical morphology for a phyllosilicate crystal, exhibiting a stair-shape pattern (Kumar et al., 2016; Sayed Hassan et al., 2006). This confirms that the Domain 4 observed by Ar adsorption can reasonably be attributed to steps on the basal surfaces. From the cross sections extracted from AFM measurements (Figure 3b), an average length and height of lepidolite crystal can be calculated (Table 3). The morphological features of lepidolite crystals, obtained by DIS calculations and by AFM measurements, are compared in Table 3. An excellent agreement between the two acquisition methods is obtained, which allow concluding that lepidolite crystals have width and length comprised between 42 and 350 nm (Table 3). This structural parameter is of paramount importance for the froth flotation process since it will influence significantly the viscosity of the pulp in the flotation cell as well as the bubble-particle attachment mechanisms, responsible for the true flotation of the lepidolite particles.

Table 3 : Comparison of lepidolite crystals morphology based on argon adsorption isotherm and atomic force microscopy

Method	Length (nm)	Height (nm)
DIS (Ar)	350	42 to 78
AFM	300	70

Nitrogen derivative adsorption isotherm

Since nitrogen is a polarisable molecule with a non-zero quadrupolar moment, examining the adsorption isotherm of nitrogen on lepidolite can give complementary information about the solid-gas interface already investigated through argon adsorption (Villiéras et al., 1997). The derivative adsorption isotherm of nitrogen, along with the DIS local adsorption isotherms modelling, are displayed on Figure 4. The DIS modelling indicated that 7 local adsorption isotherms are required to correctly fit the experimental adsorption isotherm. These local isotherms are located at $\ln(P/P_0)$ values of -16.74, -14.86, -12.96, -10.79, -8.18, -6.25, and -3.08, respectively (Figure 4 and Table 4).

First, compared to the Ar adsorption, the derivative isotherms of N_2 display a different shape and a different adsorbed volume at the monolayer (Figure 1b). This highlights the significant differences obtained when different molecular probes are used for the study of surface heterogeneities of a mineral. However, the two molecular probes (N_2 and Ar) provided similar total surface specific area, namely, 20.75 $m^2 \cdot g^{-1}$ for Ar and of 21.49 $m^2 \cdot g^{-1}$ for N_2, which is consistent. More peaks (7 instead of 5) are required to fit the N_2 derivative adsorption isotherms, which means that more adsorption sites can be described using this probe. Nevertheless, the location of the peaks in $\ln(P/P_0)$ are significantly different between N_2 and Ar, which may indicate that the adsorption sites described are different or that the affinities between the adsorption sites and the probes are different.

The N_2 derivative isotherm displays three high-energy peaks, located at $\ln(P/P_0)$ values of -16.74, -14.86, and -12.96, and four low-energy sites, located at $\ln(P/P_0)$ values of -10.79, -8.18, -6.25, and -3.08. Among those peaks, two main peaks at $\ln(P/P_0)$ of -14.9 and -10.8 can be observed, which

415 is consistent with the trend observed by previous studies for talc and kaolinite, for which two
416 prominent peaks located at values of ln(P/P_0) of around -15 and -11 were observed (Michot et al.,
417 1994; Villieras et al., 1997). In particular, the location of the most prominent peak of the derivative
418 adsorption isotherm (at ln(P/P_0) = -10.8) is in perfect agreement with studies carried out by
419 Bardot and co-workers on illite, who demonstrated that this peak corresponds to potassium
420 interfoliar cations exposed on the surface (Bardot, 1998). This peak (Domain 4) therefore
421 corresponds to the potassium interfoliar cations exposed on the lepidolite surface and is the
422 equivalent of the main peak (Domain 3) observed for Ar adsorption. Similar specific surface area
423 values (7.7 $m^2 \cdot g^{-1}$ for Ar adsorption isotherm and 8.2 $m^2 \cdot g^{-1}$ for N_2 adsorption isotherm) also
424 confirm this correspondence. Strong similarities with the N_2 derivative adsorption isotherms
425 obtained for muscovite and biotite can also be observed, with very close values of ln(P/P_0) for the
426 peaks, although the amplitude of these peaks can vary significantly (Villieras et al., 1997).
427 Meanwhile, authors tried to decipher the origin of the three local high-energy adsorption
428 isotherms (Villieras et al., 1997), located at ln(P/P_0) values of -16.74, -14.86, and -12.96. They
429 assumed that those peaks might be attributed to empty hexagonal cavities non-occupied by
430 interfoliar K^+ cations on the basal planes, although considerable difficulties to attribute these sites
431 arise for trioctahedral phyllosilicates, such as biotite or lepidolite (Villieras et al., 1997).

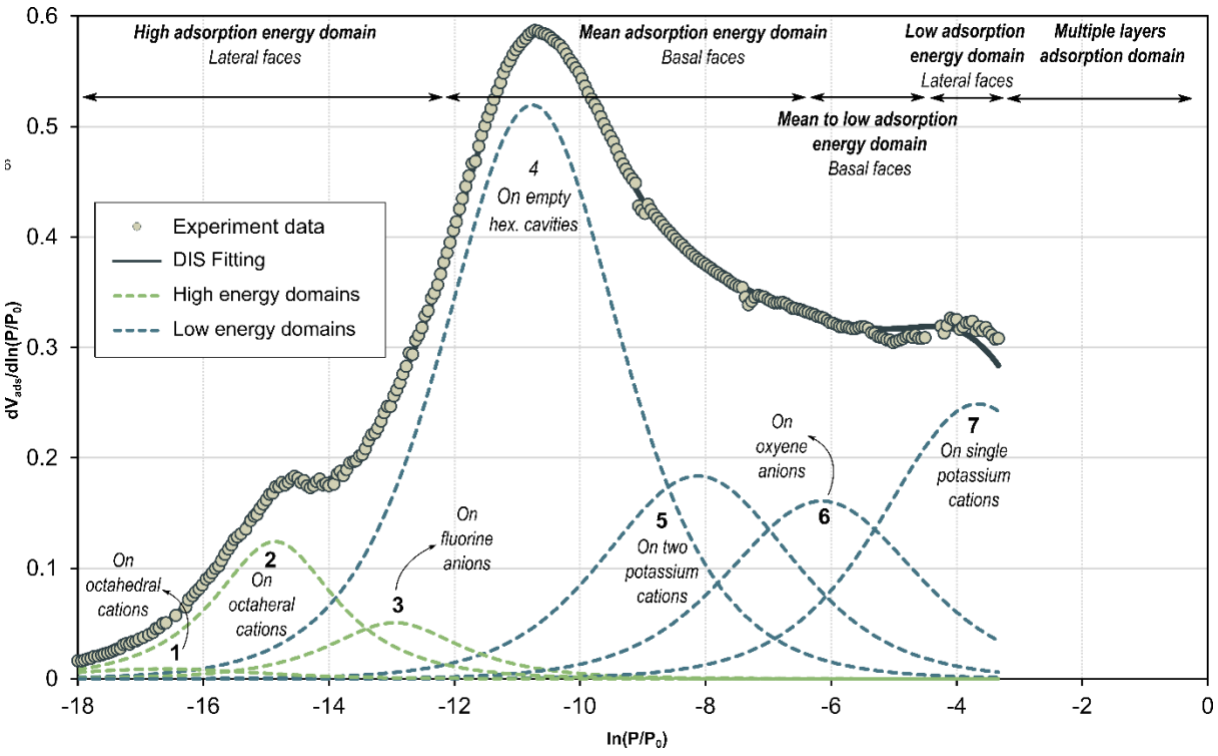

Figure 4 : First derivative of the nitrogen adsorption isotherm at 77 K on the lepidolite sample and decomposition using the DIS method. The different domains are identified with black numbers.

However, the attribution of these peaks can be discussed. According to the Ar adsorption isotherm, the basal surfaces represent a specific surface area of 16.7 $m^2 \cdot g^{-1}$ (Table 2). Based on the crystallographic features of lepidolite, as computed by Guggenheim, the surface area of a hexagonal cavity occupied by a potassium ion on the basal surface of a lepidolite crystal, *i.e.*, on the (001) crystallographic plane, is 28 $Å^2$ (Guggenheim, 1981). Again assuming that, during the cleavage process, half of the interfoliar potassium cations go on each of the two created surfaces, each K^+ cation therefore occupies 56 $Å^2$ on the basal surfaces of lepidolite. Hence, a specific surface area of basal surfaces of 16.7 $m^2 \cdot g^{-1}$ corresponds to a specific density of K^+ sites on the basal surfaces of 2.99 x 10^{19} $K^+ \cdot g^{-1}$. Considering only the three high-energy sites exhibited by the N_2 experimental adsorption isotherm and summing their contribution, a volume of 0.56 $cm^3 \cdot g^{-1}$ is related to these sites. Hence, the total number of nitrogen molecules adsorbed on those sites is 1.51 x 10^{19} molecules$\cdot g^{-1}$, which represents a half of the potassium cations calculated above. This implies that these high-energy sites correspond to either 1/4 of the total hexagonal cavities (regardless if they are occupied by a potassium cation or not), or to 1/2 of the empty hexagonal

449 cavities (*i.e.*, sites unoccupied by potassium cations). Such calculation presents a good agreement
450 with the previous studies carried out on clay minerals (Villieras et al., 1997). Also, since around
451 80% of the total surface area correspond to basal surfaces, formed by hexagonal cavities, ¼ of the
452 hexagonal cavities therefore represents 20% of the total surface area of lepidolite, which is in
453 agreement with the total volume attributed to microporosity by the BET and t-plot modelling
454 (Figure 1a). However, the contribution of these three high-energy sites in terms of specific surface
455 area (summed) only represents 2.4 $m^2 \cdot g^{-1}$ (11.1%) while, if they are ascribed to empty hexagonal
456 cavities, they should represent the same specific surface area than the potassium cations (Domain
457 4), *i.e.*, 8.2 $m^2 \cdot g^{-1}$ (38.1%), considering as many empty hexagonal cavities as potassium cations.
458 Hence, ascribing these high-energy peaks to basal surfaces is not satisfactory.

459 However, if the amount of molecules adsorbed on the main peak of the N_2 derivative isotherm are
460 compared to the amount of molecules adsorbed on the other sites, Domains 5 and 7 could
461 correspond to the adsorption of N_2 in the empty hexagonal cavities of the basal surfaces, since
462 they represent 39.1% of the total surface specific area. The presence of two different peaks for the
463 hexagonal cavities could be related to the adsorption mechanisms of N_2 on the hexagonal cavities.
464 Interestingly, some authors suggested three different mechanisms for the adsorption of N_2 on the
465 basal surfaces of phyllosilicates. These three mechanisms could correspond to the three peaks
466 observed on the N_2 derivative adsorption isotherm for basal surfaces: (1) the adsorption in empty
467 hexagonal cavities, (2) the adsorption on a single interfoliar cation, and (3) the adsorption on two
468 interfoliar cations that are closed from each other (Michot and Villiéras, 2002). Considering the
469 fact that half of the hexagonal cavities are empty, the peak at $\ln(P/P_0)$ could therefore correspond
470 to the empty hexagonal cavities while the two low-energy peaks, at $\ln(P/P_0)$ = -8.18 and $\ln(P/P_0)$
471 = -3.08 could correspond to the two different adsorption possibilities on hexagonal cavities
472 occupied by interfoliar potassium cations. More in-depth investigations are however required to
473 decipher the hypothetic attributions of those peaks.

474 *Table 4: Parameters obtained by the DIS simulation for the N_2 adsorption derivative isotherm, surface area per domain (in*
475 *absolute value and in percentage of the total specific surface area), and attribution of the different peaks to types of surfaces*
476 *and to surface adsorption sites.*

	Domain 1	Domain 2	Domain 3	Domain 4	Domain 5	Domain 6	Domain 7
$\ln(P/P_0)$	-16.74	-14.86	-12.96	-10.79	-8.18	-6.25	-3.08
ω/kT	0	1.3	1	0.3	-0.2	0.2	0
Surface ($m^2 \cdot g^{-1}$)	0.2	1.4	0.8	8.2	3.7	2.5	4.7
Surface (%)	0.9	6.5	3.7	38.1	17.2	11.6	21.9
Attribution hypothesis	Octahedral cations	Octahedral cations	Fluorine anions	Empty hex. cavities	On two potassium cations	Oxygen anions	On single potassium cation
Type of surface	Lateral	Lateral	Lateral	Basal	Basal	Lateral	Basal

Besides, the two local adsorption isotherms, located at values of $\ln(P/P_0)$ of -16.74 and -12.96 represents 0.9% and 3.7%, respectively, of the total specific surface area. Those two local isotherms can clearly be attributed to lateral surfaces, considering their high energy and their low contribution to the total specific surface area. Also, based on their ratio of surface contribution and on the crystallographic features of lepidolite, those two local isotherms can be ascribed to the adsorption of N_2 on aluminum and lithium cations of the octahedra, which are known to be exposed on the lateral surfaces. Two processes as the one identified for potassium cations might exist, considering the properties of nitrogen. Hence, these two peaks are suggested to belong to octahedral cations. Meanwhile, the peaks located at $\ln(P/P_0)$ value of -16.74 and -14.86 could also be attributed to lateral surfaces and most probably to the oxygen and fluorine anions from the octahedra and the tetrahedra, which are exposed on the lateral surfaces. Based on their relative surface contribution and on the crystallographic features of lepidolite, the peak at $\ln(P/P_0)$ = -12.96 is probably related to the adsorption of N_2 on fluorine atoms while the peak at $\ln(P/P_0)$ = -6.25 corresponds to the oxygen atoms (that are probably protonated during the cleavage process).

3.3. Additionnal insights from the solid-liquid interface

3.3.1. Electrophoretic mobility

The evolution of the zeta potential of lepidolite as a function of pH in KCl background electrolyte is displayed in Figure 5. This figure exhibits a typical trend of zeta potential variations as a function of pH, with positive values at low pH and decreasing values when the pH is increased. Lepidolite follows the same trend than other phyllosilicates, exhibiting a negative zeta potential for pH values above 3. Interestingly, a plateau is obtained at about pH 5, with constant zeta potential values around -30 mV (Figure 5).

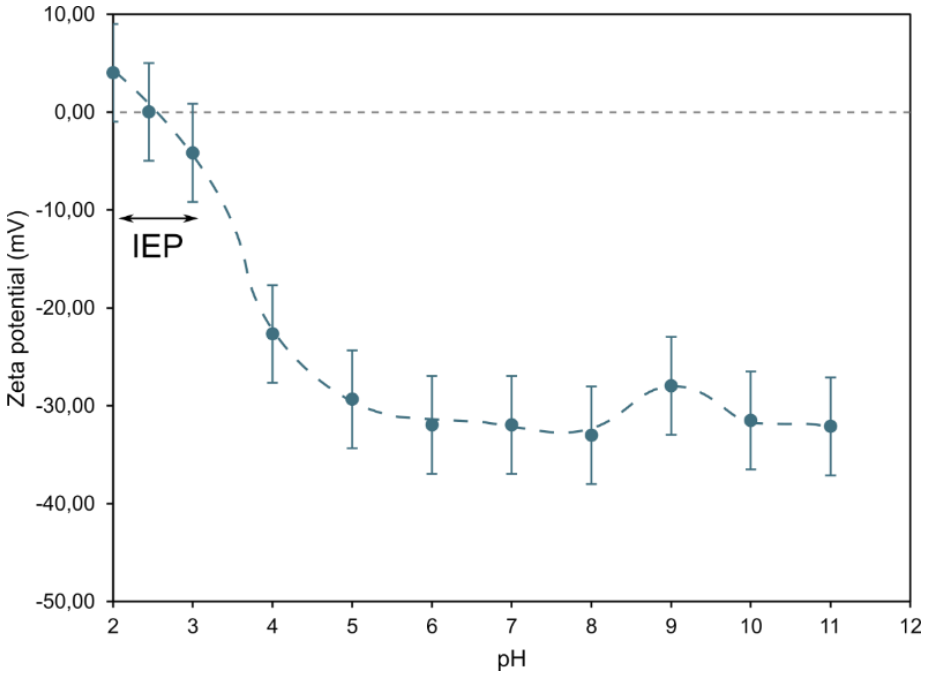

Figure 5 : Lepidolite zeta potential measurement in a KCl background electrolyte with concentration of 0.1 mol·L^{-1}. The error bars represent 2σ, σ being the standard deviation. A dashed line is plotted for easier reading.

The isoelectric point of this lepidolite sample is obtained for pH values between 2 and 3, which is a typical result in agreement with other studies carried out on lepidolite (Choi et al., 2012; Filippov et al., 2022; Wei et al., 2021), although most of these studies measured lepidolite's IEP without considering the effect of the ionic strength. Meanwhile, the electrophoretic mobility measurements at pH values of about 2 to 3 or below should be conducted with a KCl concentration of 1 x 10^{-1} mol·L^{-1}, to avoid a significant variation in the ionic strength induced by the pH modification. Hence, Figure 5 displays electrophoretic mobility measurement for this concentration of KCl only. With this test, IEP highlighted by previous studies is confirmed (Figure 5).

3.3.2. Surface titration

PZC determination

Although several surface titrations at different ionic strengths were performed (Figure 6), the determination of the PZC of lepidolite remains a matter of discussion. The trend obtained for lepidolite was in agreement with what was observed for kaolinite, montmorillonite and talc (Burdukova et al., 2007; Duc et al., 2006; Kraepiel et al., 1998; Mbey et al., 2019). In particular, Delhorme and co-workers highlighted, using modelling, that this trend was related to the permanent layer charge of phyllosilicates (Delhorme et al., 2010). The permanent layer charge of lepidolite presents a value of 0.9-1.0, very close to the one of muscovite and biotite, which is known to be one of the greatest layer charge for phyllosilicates (Bergaya et al., 2011; Giese, 1978). However, from Figure 6, it appears that the pH value at which the curves of the net proton consumption have a zero value converges around 8.5, with an increasing background electrolyte concentration. Since a background electrolyte of 100 $mol \cdot L^{-1}$ represents a significant ionic strengh, it can be suggested that the PZC of lepidolite should be in an order of magnitude close to 8.5. Authors proposed the use of the Mular–Roberts titration method to record phyllosilicates PZC (Alvarez-Silva et al., 2010a, 2010b) while neglecting the permanent layer charge of this type of minerals. Based on these methods, they demonstrated that the PZC of anisotropic minerals such as phyllosilicates is usually considerably above the IEP of these minerals, which further confirms the fact that PZC of lepidolite is much higher than its IEP. Finally, Burdukova and co-authors tried attributing this specific behaviour of titration curves, for talc crystals, to the contribution of both basal and edges surfaces (Burdukova et al., 2007). From these observations, traditional consideration of the surface properties of this clay-like mineral can be reconsidered, such as considering the IEP of lepidolite being the PZC.

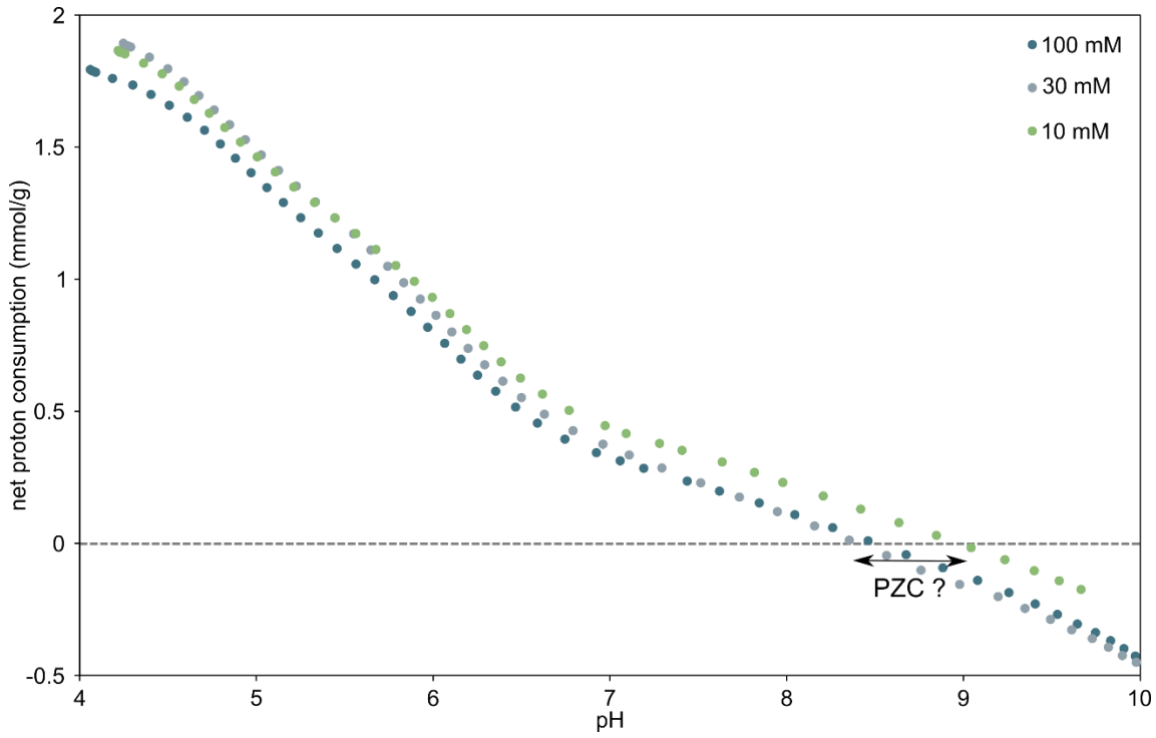

Figure 6: Net proton consumption as a function of the pH for the lepidolite sample, with different values of ionic strength. Thus procedure was used to determine the PZC of the lepidolite sample used in this study. The KNO_3 background electrolyte has concentration of 10, 30 and 100 mM.

TDIS: Surface pKa determination

The raw titration curves converted into surface net proton consumption, for two duplicated tests, are presented in Figure 7. The mean absolute error (MAE), which is the preferred statistic estimator when low and/or negative values are considered (Hyndman and Koehler, 2006; Morley et al., 2018; Swanson et al., 2000; Tofallis, 2015), was computed between these two tests. This error represents the average absolute difference of the net proton consumption for a given pH value between the two tests. From this figure, the repeatability of the titration can be assessed and is very good, since the MAE is of about 0.1.

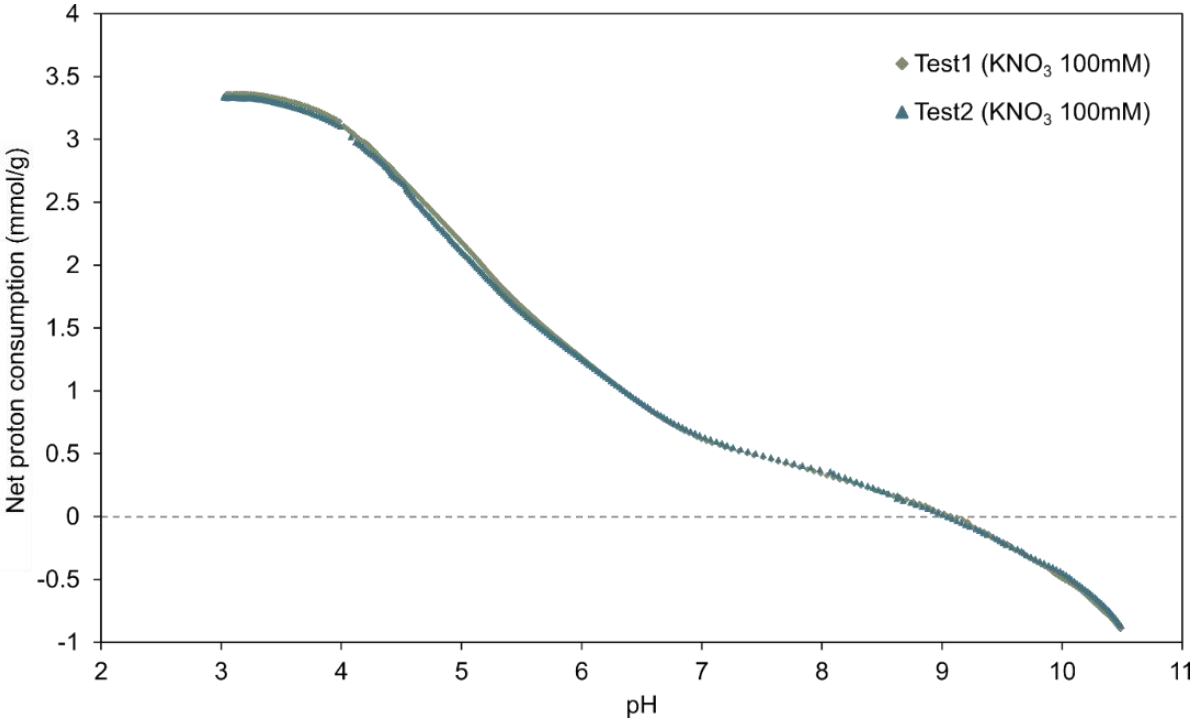

Figure 7: Lepidolite net proton consumption in a 100mM KNO_3 background electrolyte. Conversion of two raw titration curves, showing the good repetability of the data acquired (titration 1 and 2).

The TDIS method was used to determine the pKa values of the different reactive sites present in the solution. Since the contribution of the background electrolyte was removed, the obtained titration curve and its derivative only originated from the contribution of the different surface acid-base sites of the lepidolite. The processing of this derivative curve using the TDIS method allowed obtaining the peaks that represented the distribution of the lepidolite surface sites (Figure 8). Two prominent peaks, at pH values of around 5 and 6.5, respectively, can be clearly observed on the derivative curve, along with a third peak starting at pH 9 and expanding to a region that is not covered by the pH range studied.

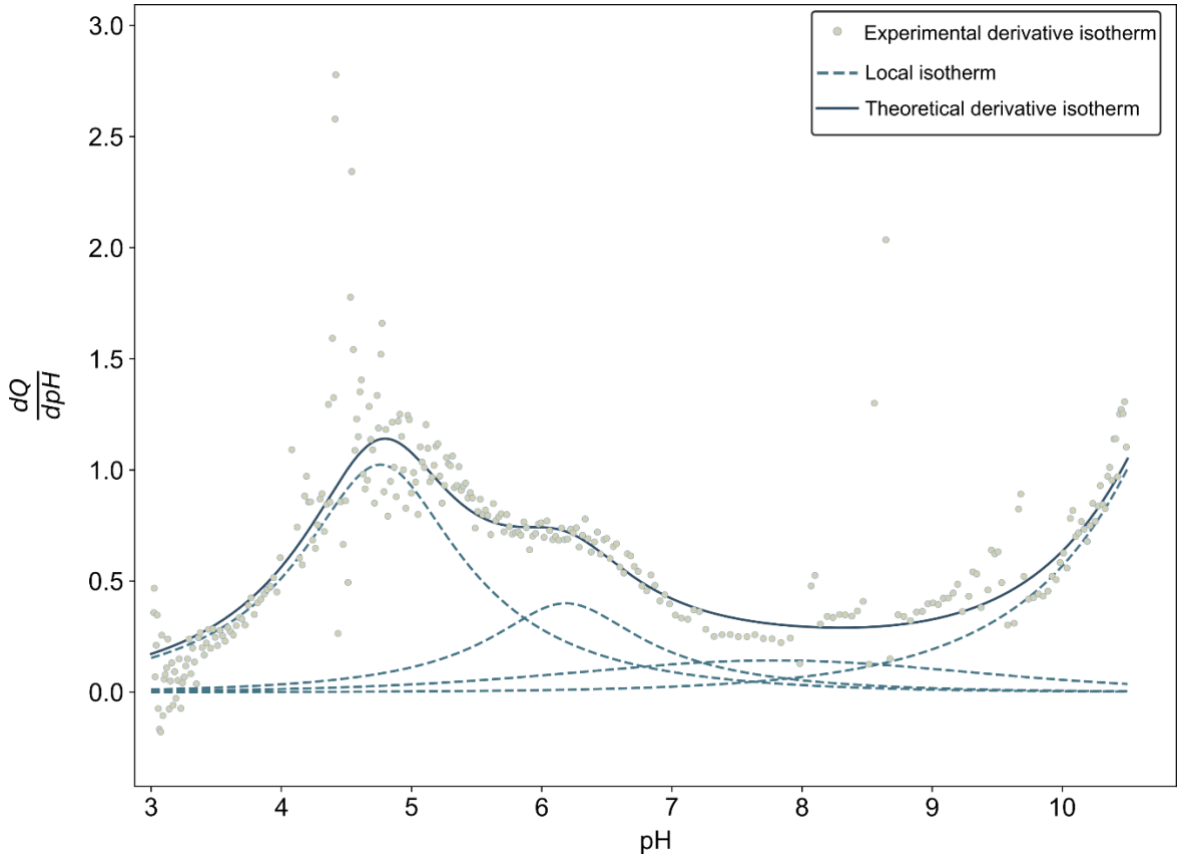

557

558 *Figure 8: Experimental derivative hydroxyl adsorption isotherm obtained at 0.1 mol·L^{-1} KNO_3 on lepidolite along with the*
559 *hydroxyl/proton affinity distribution using the TDIS procedure.*

560 Using the TDIS method and the optimized parameters based on the PEST software, a minimum of
561 four local theoretical isotherms are required to obtain a good fit of the experimental derivative
562 (Table 5).

563 *Table 5: Peak position (in pH values) of the four theoretical isotherms used to predict the experimental derivative using the*
564 *TDIS approach, along with their contribution to the total measured surface reactivity, and their attribution in terms of*
565 *surface sites and in terms of type of surfaces.*

	Domain 1	Domain 2	Domain 3	Domain 4
pH value	4.8	6.2	7.8	11.5
Surface (%)	60.2	22.6	17.2	N/A
Attribution hypothesis	Oxygen atoms from silicon tetrahedra	Oxygen atoms from aluminum tetrahedra	Oxygen atoms from lateral surfaces	N/A
Type of surface	Basal	Basal	Lateral	N/A

As stated above, these four local isotherms correspond to the adsorption of protons by four surface sites of the lepidolite. Since these local isotherms are symmetric regarding the position of their maximum, this position corresponds to the pH value at which half of the sites are protonated and half are deprotonated. Hence, the abscissa values of these peaks exactly represent the pKa of the reactive sites. Three different acid-base sites are therefore exhibited on the surface of lepidolite, with pKa values of 4.8, 6.2, and 7.8. Meanwhile, no conclusion can be drawn for the last peak (located at pH 11.5) since it can either express a possible surface pKa at values above 10 or be linked to possible noise during the acquisition of the last points, considering the high values of pH in this range.

By considering the area under each peak, the contribution of each acid-base site to the surface reactivity towards protons can be determined. The peak at a pH value of 4.8 is the most important one, with a contribution of 60.2%, directly followed by the peak at pH 6.2, which represents 22.6%. The last peak, located at pH 7.8, corresponds to 17.2% of the total surface reactivity. Only the three main peaks are considered since the last, located at pH 11.5, could be attributed to noise due to (i) experimental acquisition of potential in alkali conditions, (ii) experimental derivative of noisy data, or (iii) mineral dissolution, commonly observed at alkaline pH.

The three peaks and their correspondence in terms of surface groups and surface types are discussed in the next section. Based on these results, the two first peaks, located at pH 4.8 and 6.2, represent 82.8% of the total surface reactivity and most probably correspond to the basal surfaces. This is in perfect agreement with the results of Ar and N_2 adsorption experiments, which allowed determining a total contribution of the basal surfaces 80.8% and 77.2% to the total specific surface area of this lepidolite sample. This induces that the surface pKa located at a pH 7.8 can be attributed to a surface site that is part of lateral surfaces, since its contribution represents around 17.2% of the total surface reactivity. This peak is very broad, which is probably related to various contributions in this peak, corresponding to the diversity of the reactive sites on the lateral surfaces (fluorine atoms, oxygen atoms from lithium octahedra, oxygen atoms from

aluminum octahedra, hydroxyl groups…). Interestingly, the two surface sites ascribed to basal surfaces represent 75% and 25%, respectively, of the total basal groups. Based on the cation ordering calculated by Guggenheim in 1981, this perfectly represents the ratio of Si-O and Al-O in tetrahedral crystallographic sites of lepidolite (Guggenheim, 1981). Hence, these pKa values can represent either actual sites that can be protonated/deprotonated or, considering the permanent layer charge of micas and the fact that these sites are in complete coordination, pH values at which interfoliar potassium can leach from or bind to the basal surface of micas. On overall, the adsorption of protons (or hydroxyl groups) on the surface demonstrates that the potassium interfoliar cations, exposed on the lepidolite basal surfaces, are released to the water bulk. This means that the surface acid-base reactions are related to a cation exchange, *i.e.*, the release of a potassium cation that allows the adsorption of a proton. To better characterize the peaks exhibited by surface titration, their pKa values could be compared to values obtained for pure SiO_2 and pure Al_2O_3. The point of zero charge of silica is usually recorded at a pH value of about 3 (Kosmulski, 2001), which means that surface sites are hydroxylated at pH 3 and that pKa values can be exhibited at lower and higher pH values. Thus, the surface pKa value at pH 4.8 could represent the pKa of the following reaction:

$$Si\text{-}OH \leftrightarrows Si\text{-}O^- + H^+ \quad (3)$$

Such value for this pKa is an excellent agreement with pKa values calculated for silanol groups on quartz surface by surface titration and second harmonic generation methods, since values ranging from 4.5 to 5.5 were reported (Allen et al., 1971; Ong et al., 1992). Meanwhile, the pKa of the second protonation reaction of silanol sites could not be recorded: studies conducted on pure silica suggested that this second protonation reaction of silanol groups generally occurs at pH value below -2 (Liu et al., 2014), which is out of the pH range investigated in this work. In the same idea, the PZC of alumina species is commonly determined at pH values of about 8-9 (Kosmulski, 2001; Sposito, 1996). Therefore, the pKa recorded at 6.2 in this work could represent the second protonation of alumina sites:

$$Al\text{-}OH_2^+ \leftrightarrows Al\text{-}OH + H^+ \quad (4)$$

Conclusions

In this comprehensive study, we carried out an in-depth analysis of lepidolite surfaces, the main lithium-bearing phyllosilicate mineral exploited for lithium extraction, based on solid-gas and solid-liquid interfaces analyses. By the combination of various analytical techniques, including nitrogen and argon adsorption isotherms, electrophoretic mobility measurements, and surface potentiometric titration, we provided insights into the surface properties of lepidolite. First, the adsorption of Ar and N_2 as well as the surface titration exhibited the dominance of the basal surfaces over the lateral surfaces in the total specific surface area, representing 77-82% and 18-23% of the total specific surface area, respectively. The two molecular probes used for gas adsorption isotherm(N_2 and Ar) allowed discussing in details the crystallographic sites exposed on the lepidolite surfaces and better understand their role in the adsorption. Meanwhile, the electrophoretic mobility measurements demonstrated an IEP between pH 2 and 3, while potentiometric surface titration experiments provided a PZC at around 8.5, highlighting the significant difference between IEP and PZC for lepidolite. Also, surface titration experiments revealed the presence of acid-base surface sites presenting pKa values of 4.8, 6.2, and 7.8, which were attributed to the exposed oxygen atoms of the silicon tetrahedra, of the aluminum tetrahedra, and of the various octahedra, respectively. The implications of these findings for the flotation separation process are noteworthy, as they provide potential avenues for the selective separation of lepidolite from other silicate minerals, reducing costs. Based on selective adsorption of cationic and anionic surfactant mixture, it might be possible to separate phyllosilicates from usual silicate minerals. This selective adsorption might be linked to the PZC of lepidolite being of about 7-9. In these conditions, it should be possible to selectively adsorb both cationic and anionic reagents at the lepidolite surface, since its surface will exhibit equal proportion of positive, neutral and negative surface sites. This route allows selectivity between close minerals in neutral pH values using green reagents (sodium oleate or lignin sulfonate). On overall, this research provided valuable data to understanding lepidolite's surface properties and highlights opportunities for

more efficient mineral processing techniques. The surface characterization and insights thrown for this study open the door to further exploration and application of these findings in mineral beneficiation processes, with the potential for substantial economic and environmental benefits.

Acknowledgement

The authors acknowledge Sébastien Martineau and Dagan Mace from Ecole Nationale Supérieure de Géologie (Nancy, France) for their support and help for the definition of the experimental setup. We acknowledge the support of Labex Ressources 21 supported by the French National Research Agency through the national program "Investissements d'Avenir" [reference ANR–10–LABX–21-01]. Experiments leading to this publication were performed at the STEVAL (Station Expérimentale de Valorisation des ressources minérales et des substances residuaires) facility. This work was partly carried out in the Pôle de compétences Physico-Chimie de l'Environnement, LIEC laboratory UMR 7360 CNRS- Université de Lorraine. Ultimately, this publication is following results from previous PhD theses, namely the ones of J.M. Cases (1967), L.Michot (1994), F. Bardot (1998), and B. Prelot (2001).

References

1. Allen, L.H., Matijevíc, E., Meites, L., 1971. Exchange of Na+ for the silanolic protons of silica. Journal of Inorganic and Nuclear Chemistry 33, 1293–1299. https://doi.org/10.1016/0022-1902(71)80423-2
2. Alvarez-Silva, M., Mirnezami, M., Uribe-Salas, A., Finch, J.A., 2010a. Point of Zero Charge, Isoelectric Point and Aggregation of Phyllosilicate Minerals. Canadian Metallurgical Quarterly 49, 405–410. https://doi.org/10.1179/cmq.2010.49.4.405
3. Alvarez-Silva, M., Uribe-Salas, A., Mirnezami, M., Finch, J.A., 2010b. The point of zero charge of phyllosilicate minerals using the Mular–Roberts titration technique. Minerals Engineering 23, 383–389. https://doi.org/10.1016/j.mineng.2009.11.013
4. Antti, B.-M., Forssberg, E., 1989. Pulp chemistry in industrial mineral flotation. Studies of surface complex on calcite and apatite surfaces using FTIR spectroscopy. Minerals Engineering 2, 217–227. https://doi.org/10.1016/0892-6875(89)90042-3
5. Bergaya, F., Jaber, M., Lambert, J., 2011. Clays and clay minerals. Rubber-Clay Nanocomposites: Science, Technology, and Applications 1–44. https://doi.org/10.1002/9781118092866.ch1
6. Brantley, S.L., Mellott, N.P., 2000. Surface area and porosity of primary silicate minerals. American Mineralogist 85, 1767–1783. https://doi.org/10.2138/am-2000-11-1220
7. Brunauer, S., Emmett, P.H., Teller, E., 1938. Adsorption of Gases in Multimolecular Layers. J. Am. Chem. Soc. 60, 309–319. https://doi.org/10.1021/ja01269a023

8. Brus, J., Milena Špírková, Hlavatá, D., Strachota, A., 2004. Self-Organization, Structure, Dynamic Properties, and Surface Morphology of Silica/Epoxy Films As Seen by Solid-State NMR, SAXS, and AFM. Macromolecules 37, 1346–1357. https://doi.org/10.1021/ma035608h
9. Buckton, G., 2000. Interfacial Phenomena in Drug Delivery and Targeting. CRC Press. https://doi.org/10.1201/9781482296785
10. Burdukova, E., Becker, M., Bradshaw, D.J., Laskowski, J.S., 2007. Presence of negative charge on the basal planes of New York talc. Journal of colloid and interface science 315, 337–342. https://doi.org/10.1016/j.jcis.2007.06.067
11. Cabrera, F., 1979. The Release of Aluminum from Aluminosilicate Minerals. II. Acid-Base Potentiometric Titrations. Clays and Clay Minerals 27, 113–118. https://doi.org/10.1346/CCMN.1979.0270206
12. Cases, J.-M., Villiéras, F., Michot, L., 2000. Les phénomènes d'adsorption, d'échange ou de rétention à l'interface solide–solution aqueuse.1. Connaissance des propriétés structurales, texturales et superficielles des solides. Comptes Rendus de l'Académie des Sciences - Series IIA - Earth and Planetary Science 331, 763–773. https://doi.org/10.1016/S1251-8050(00)01495-6
13. Charmas, B., Leboda, R., Gérard, G., Villiéras, F., 2002. Effects of oxidation on surface heterogeneity of carbosils. Applied Surface Science 196, 126–137. https://doi.org/10.1016/S0169-4332(02)00044-2
14. Chatman, S., Zarzycki, P., Preočanin, T., Rosso, K.M., 2013. Effect of surface site interactions on potentiometric titration of hematite (α-Fe2O3) crystal faces. Journal of Colloid and Interface Science 391, 125–134. https://doi.org/10.1016/j.jcis.2012.09.081
15. Choi, J., Kim, W., Chae, W., Kim, S.B., Kim, H., 2012. Electrostatically Controlled Enrichment of Lepidolite via Flotation. Mater. Trans. 53, 2191–2194. https://doi.org/10.2320/matertrans.M2012235
16. Christmann, P., Gloaguen, E., Labbé, J.-F., Melleton, J., Piantone, P., 2015. Global Lithium Resources and Sustainability Issues, in: Lithium Process Chemistry. Elsevier, pp. 1–40. https://doi.org/10.1016/B978-0-12-801417-2.00001-3
17. Churakov, S.V., Armbruster, T., Danisi, R.M., 2015. Ab initio simulations of mineral surfaces: Recent advances in numerical methods and selected applications. Highlights in Mineralogical Crystallography 75–108. https://doi.org/10.1515/9783110417104-005
18. De Boer, J.H., Lippens, B.C., Linsen, B.G., Broekhoff, J.C.P., Van Den Heuvel, A., Osinga, Th.J., 1966. Thet-curve of multimolecular N2-adsorption. Journal of Colloid and Interface Science 21, 405–414. https://doi.org/10.1016/0095-8522(66)90006-7
19. Delhorme, M., Labbez, C., Caillet, C., Thomas, F., 2010. Acid–Base Properties of 2:1 Clays. I. Modeling the Role of Electrostatics. Langmuir 26, 9240–9249. https://doi.org/10.1021/la100069g
20. Dell'Angelo, D., Lainé, J., Said, H., Foucaud, Y., Badawi, M., 2024. Machine Learning Force Field beyond the Limits of Classical and First-Principles Molecular Dynamics Simulations: The Case of Kaolinite Hydration. J. Phys. Chem. C 128, 11447–11455. https://doi.org/10.1021/acs.jpcc.4c03288
21. Deng, Y., Ou, L., 2024. Mechanism for the selective separation of lepidolite from albite by sodium lauroyl glutamate as a green environment collector. Colloids and Surfaces A: Physicochemical and Engineering Aspects 701, 134922. https://doi.org/10.1016/j.colsurfa.2024.134922
22. Doherty, J., 2015. Calibration and Uncertainty Analysis for Complex Environmental Models. Watermark Numerical Computing, Brisbane, Australia. DOI:10.1111/gwat.12360
23. Duc, M., Thomas, F., Gaboriaud, F., 2006. Coupled chemical processes at clay/electrolyte interface: A batch titration study of Na-montmorillonites. Journal of Colloid and Interface Science 300, 616–625. https://doi.org/10.1016/j.jcis.2006.04.081

24. Elmi, C., Brigatti, M.F., Guggenheim, S., Pasquali, L., Montecchi, M., Nannarone, S., 2014. Crystal chemistry and surface configurations of two polylithionite-1M crystals. American Mineralogist 99, 2049–2059. https://doi.org/10.2138/am-2014-4908
25. Faris, N., Ram, R., Tardio, J., Bhargava, S., McMaster, S., Pownceby, M.I., 2017. Application of ferrous pyrometallurgy to the beneficiation of rare earth bearing iron ores – A review. Minerals Engineering 110, 20–30. https://doi.org/10.1016/j.mineng.2017.04.005
26. Farrokhpay, S., Filippov, L., Fornasiero, D., 2021. Flotation of Fine Particles: A Review. Mineral Processing and Extractive Metallurgy Review 42, 473–483. https://doi.org/10.1080/08827508.2020.1793140
27. Filippov, L.O., Filippova, I.V., Crumiere, G., Sousa, R., Leite, M.M., de Sousa, A.B., Korbel, C., Tripathy, S., 2022. Separation of lepidolite from hard-rock pegmatite ore via dry processing and flotation. https://doi.org/10.1016/j.mineng.2022.107768
28. Foucaud, Y., Badawi, M., Filippov, L., Filippova, I., Lebègue, S., 2019. A review of atomistic simulation methods for surface physical-chemistry phenomena applied to froth flotation. Minerals Engineering 143, 106020. https://doi.org/10.1016/j.mineng.2019.106020
29. Foucaud, Y., Lebègue, S., Filippov, L.O., Filippova, I.V., Badawi, M., 2018. Molecular Insight into Fatty Acid Adsorption on Bare and Hydrated (111) Fluorite Surface. J. Phys. Chem. B 122, 12403–12410. https://doi.org/10.1021/acs.jpcb.8b08969
30. Foucaud, Y., Siboulet, B., Duvail, M., Jonchere, A., Diat, O., Vuilleumier, R., Dufrêche, J.-F., 2021. Deciphering second harmonic generation signals. Chemical Science 12, 15134–15142. https://doi.org/10.1039/D1SC03960A
31. Fukushi, K., Sverjensky, D.A., 2007. A surface complexation model for sulfate and selenate on iron oxides consistent with spectroscopic and theoretical molecular evidence. Geochimica et Cosmochimica Acta 71, 1–24. https://doi.org/10.1016/j.gca.2006.08.048
32. Gao, Z., Sun, W., Hu, Y., 2014. Mineral cleavage nature and surface energy: Anisotropic surface broken bonds consideration. Transactions of Nonferrous Metals Society of China 24, 2930–2937. https://doi.org/10.1016/S1003-6326(14)63428-2
33. Giese, R.F., 1978. The Electrostatic Interlayer Forces of Layer Structure Minerals. Clays and Clay Minerals 26, 51–57. https://doi.org/10.1346/CCMN.1978.0260106
34. Gorain, B.K., 2013. Developing solutions to complex flotation problems, in: Proceedings of the 34th Canadian Mineral Processors Conference. pp. 293–312. Available: OneMine | Developing Solutions To Complex Flotation Problems (INTERNATIONAL MINERAL PROCESSING CONGRESS (IMPC) 2012 PROCEEDINGS / NEW DELHI, INDIA)
35. Gourcerol, B., Gloaguen, E., Melleton, J., Tuduri, J., Galiegue, X., 2019. Re-assessing the European lithium resource potential – A review of hard-rock resources and metallogeny. Ore Geology Reviews 109, 494–519. https://doi.org/10.1016/j.oregeorev.2019.04.015
36. Gregg S. J., Sing K. S. W. and Salzberg H.W., 1967. Adsorption Surface Area and Porosity. Journal of The Electrochemical Society 114, 279Ca. DOI 10.1149/1.2426447
37. Guggenheim, S., 1981. Cation ordering in lepidolite. American Mineralogist 66, 1221–123. Available: Cation ordering in lepidolite | American Mineralogist | GeoScienceWorld
38. Hudec, P., Smiešková, A., Idek, Z., Schneider, P., Ŝolcová, O., 2002. Determination of microporous structure of zeolites by t-plot method—State-of-the-art, in: Studies in Surface Science and Catalysis. Elsevier, pp. 1587–1594. https://doi.org/10.1016/S0167-2991(02)80328-7
39. Hyndman, R.J., Koehler, A.B., 2006. Another look at measures of forecast accuracy. International Journal of Forecasting 22, 679–688. https://doi.org/10.1016/j.ijforecast.2006.03.001
40. Kesler, S.E., Gruber, P.W., Medina, P.A., Keoleian, G.A., Everson, M.P., Wallington, T.J., 2012. Global lithium resources: Relative importance of pegmatite, brine and other deposits. Ore Geology Reviews 48, 55–69. https://doi.org/10.1016/j.oregeorev.2012.05.006

41. Kleeberg, R., Monecke, T., Hillier, S., 2008. Preferred Orientation of Mineral Grains in Sample Mounts for Quantitative XRD Measurements: How Random are Powder Samples? Clays Clay Miner. 56, 404–415. https://doi.org/10.1346/CCMN.2008.0560402
42. Korbel, C., Filippova, I., Filippov, L., 2023. Froth flotation of lithium micas–A review. Minerals Engineering 192, 107986. https://doi.org/10.1016/j.mineng.2022.107986
43. Kosmulski, M., 2001. Chemical properties of material surfaces. CRC press. https://doi.org/10.1201/9780367800482
44. Kraepiel, A.M., Keller, K., Morel, F.M., 1998. On the acid− base chemistry of permanently charged minerals. Environmental Science & Technology 32, 2829–2838. https://doi.org/10.1021/es9802899
45. Krog, N., Barfod, N. m., Sanchez, R. m., 1989. Interfacial phenomena in food emulsions. Journal of Dispersion Science and Technology 10, 483–504. https://doi.org/10.1080/01932698908943185
46. Kumar, N., Zhao, C., Klaassen, A., Van Den Ende, D., Mugele, F., Siretanu, I., 2016. Characterization of the surface charge distribution on kaolinite particles using high resolution atomic force microscopy. Geochimica et Cosmochimica Acta 175, 100–112. https://doi.org/10.1016/j.gca.2015.12.003
47. Levinson, A.A., 1953. STUDIES IN THE MICA GROUP; RELATIONSHIP BETWEEN POLYMORPHISM AND COMPOSITION IN THE MUSCOVITE-LEPIDOLITE SERIES. American Mineralogist 38, 88–107. Available: Studies in the mica group; relationship between polymorphism and composition in the muscovite-lepidolite series*† | American Mineralogist | GeoScienceWorld
48. Li, H., Eksteen, J., Kuang, G., 2019. Recovery of lithium from mineral resources: State-of-the-art and perspectives – A review. Hydrometallurgy 189, 105129. https://doi.org/10.1016/j.hydromet.2019.105129
49. Liu, X., Cheng, J., Lu, X., Wang, R., 2014. Surface acidity of quartz: understanding the crystallographic control. Phys. Chem. Chem. Phys. 16, 26909–26916. https://doi.org/10.1039/C4CP02955K
50. Lu, W.-K., Bitsianes, G., 1968. Chemical kinetics of gaseous reduction of hematite. Canadian Metallurgical Quarterly 7, 3–13. https://doi.org/10.1179/cmq.1968.7.1.3
51. Massaro, C., Rotolo, P., De Riccardis, F., Milella, E., Napoli, A., Wieland, M., Textor, M., Spencer, N.D., Brunette, D.M., 2002. Comparative investigation of the surface properties of commercial titanium dental implants. Part I: chemical composition. Journal of Materials Science: Materials in Medicine 13, 535–548. https://doi.org/10.1023/A:1015170625506
52. Mbey, J.A., Thomas, F., Razafitianamaharavo, A., Caillet, C., Villiéras, F., 2019. A comparative study of some kaolinites surface properties. Applied Clay Science 172, 135–145. https://doi.org/10.1016/j.clay.2019.03.005
53. Michot, L., François, M., Cases, J.M., 1990. Surface heterogeneity studied by a quasi-equilibrium gas adsorption procedure. Langmuir 6, 677–681. https://doi.org/10.1021/la00093a025
54. Michot, L.J., Villiéras, F., 2002. Assessment of surface energetic heterogeneity of synthetic Na- saponites. The role of layer charge. Clay miner. 37, 39–57. https://doi.org/10.1180/0009855023710016
55. Michot, L.J., Villieras, F., Francois, M., Yvon, J., Le Dred, R., Cases, J.M., 1994. The Structural Microscopic Hydrophilicity of Talc. Langmuir 10, 3765–3773. https://doi.org/10.1021/la00022a061
56. Moon, K.S., Fuerstenau, D.W., 2003. Surface crystal chemistry in selective flotation of spodumene (LiAl[SiO3]2) from other aluminosilicates. International Journal of Mineral Processing 72, 11–24. https://doi.org/10.1016/S0301-7516(03)00084-X
57. Morley, S.K., Brito, T.V., Welling, D.T., 2018. Measures of Model Performance Based On the Log Accuracy Ratio. Space Weather 16, 69–88. https://doi.org/10.1002/2017SW001669

58. Mukhopadhyay, B., Walther, J.V., 2001. Acid–base chemistry of albite surfaces in aqueous solutions at standard temperature and pressure. Chemical Geology 174, 415–443. https://doi.org/10.1016/S0009-2541(00)00288-6
59. Ong, S., Zhao, X., Eisenthal, K.B., 1992. Polarization of water molecules at a charged interface: second harmonic studies of the silica/water interface. Chemical Physics Letters 191, 327–335. https://doi.org/10.1016/0009-2614(92)85309-X
60. Papirer, E., Eckhardt, A., Muller, F., Yvon, J., 1990. Grinding of muscovite: influence of the grinding medium. J Mater Sci 25, 5109–5117. https://doi.org/10.1007/BF00580138
61. Papirer, E., Roland, P., Nardin, M., Balard, H., 1986. Variation of the surface energy characteristics of mica (muscovite) upon grinding. Journal of Colloid and Interface Science 113, 62–66. https://doi.org/10.1016/0021-9797(86)90205-5
62. Pernyeszi, T., Dékány, I., 2003. Surface fractal and structural properties of layered clay minerals monitored by small-angle X-ray scattering and low-temperature nitrogen adsorption experiments. Colloid Polym Sci 281, 73–78. https://doi.org/10.1007/s00396-002-0758-0
63. Perronnet, M., Villiéras, F., Jullien, M., Razafitianamaharavo, A., Raynal, J., Bonnin, D., 2007. Towards a link between the energetic heterogeneities of the edge faces of smectites and their stability in the context of metallic corrosion. Geochimica et Cosmochimica Acta 71, 1463–1479. https://doi.org/10.1016/j.gca.2006.12.011
64. Pinto, F.G., Junior, R.E., Saint'Pierre, T.D., 2012. Sample Preparation for Determination of Rare Earth Elements in Geological Samples by ICP-MS: A Critical Review. Analytical Letters 45, 1537–1556. https://doi.org/10.1080/00032719.2012.677778
65. Prélot, B., Charmas, R., Zarzycki, P., Thomas, F., Villiéras, F., Piasecki, W., Rudziński, W., 2002. Application of the Theoretical 1-p *K* Approach to Analyzing Proton Adsorption Isotherm Derivatives on Heterogeneous Oxide Surfaces. J. Phys. Chem. B 106, 13280–13286. https://doi.org/10.1021/jp0200573
66. Ramsey, M.H., Potts, P.J., Webb, P.C., Watkins, P., Watson, J.S., Coles, B.J., 1995. An objective assessment of analytical method precision: comparison of ICP-AES and XRF for the analysis of silicate rocks. Chemical Geology 124, 1–19. https://doi.org/10.1016/0009-2541(95)00020-M
67. Ratner, B.D., Castner, D.G., 2020. Surface Properties and Surface Characterization of Biomaterials, in: Biomaterials Science. Elsevier, pp. 53–75. https://doi.org/10.1016/B978-0-12-816137-1.00006-4
68. Richardson, F.D., 1982. Interfacial phenomena and metallurgical processes. Canadian Metallurgical Quarterly 21, 111–119. https://doi.org/10.1179/cmq.1982.21.2.111
69. Roy, S., 2009. Recovery Improvement of Fine Iron Ore Particles by Multi Gravity Separation. TOMPJ 2, 17–30. https://doi.org/10.2174/1874841400902010017
70. Sahoo, S.K., Tripathy, S.K., Nayak, A., Hembrom, K.C., Dey, S., Rath, R.K., Mohanta, M.K., 2022. Beneficiation of lithium bearing pegmatite rock: a review. Mineral Processing and Extractive Metallurgy Review 1–27. https://doi.org/10.1080/08827508.2022.2117172
71. Salvador, F., Sánchez-Jiménez, C., Sánchez-Montero, M.J., Salvador, A., 2002. A review of the application of the BET equation to experimental data: the C parameter, in: Studies in Surface Science and Catalysis. Elsevier, pp. 379–386. https://doi.org/10.1016/S0167-2991(02)80158-6
72. Sayed Hassan, M., Villieras, F., Gaboriaud, F., Razafitianamaharavo, A., 2006. AFM and low-pressure argon adsorption analysis of geometrical properties of phyllosilicates. Journal of Colloid and Interface Science 296, 614–623. https://doi.org/10.1016/j.jcis.2005.09.028
73. Silva, A.L. da, Oliveira, A.H. de, Fernandes, M.L.S., 2011. Influence of preferred orientation of minerals in the mineralogical identification process by X-ray diffraction. Presented at the International Nuclear Atlantic Conference, Belo Horizonte,MG, Brazil. Available: Influence of preferred orientation of minerals in the mineralogical identification process by X-ray diffraction (Conference) | ETDEWEB

74. Sing, K.S., 1985. Reporting physisorption data for gas/solid systems with special reference to the determination of surface area and porosity (Recommendations 1984). Pure and applied chemistry 57, 603–619. https://doi.org/10.1351/pac198557040603
75. Smoluchowski, M. v, 1918. Versuch einer mathematischen Theorie der Koagulationskinetik kolloider Lösungen. Zeitschrift für physikalische Chemie 92, 129–168. https://doi.org/10.1515/zpch-1918-9209
76. Sposito, G. (Ed.), 1996. The environmental chemistry of aluminum, 2. ed. ed. Lewis Publishers, Boca Raton. https://doi.org/10.1201/9780138736781
77. Storck, S., Bretinger, H., Maier, W.F., 1998. Characterization of micro- and mesoporous solids by physisorption methods and pore-size analysis. Applied Catalysis A: General 174, 137–146. https://doi.org/10.1016/S0926-860X(98)00164-1
78. Swanson, D.A., Tayman, J., Barr, C.F., 2000. A note on the measurement of accuracy for subnational demographic estimates. Demography 37, 193–201. https://doi.org/10.2307/2648121
79. Szekeres, M., Tombácz, E., 2012. Surface charge characterization of metal oxides by potentiometric acid–base titration, revisited theory and experiment. Colloids and Surfaces A: Physicochemical and Engineering Aspects 414, 302–313. https://doi.org/10.1016/j.colsurfa.2012.08.027
80. Tadesse, B., Makuei, F., Albijanic, B., Dyer, L., 2019. The beneficiation of lithium minerals from hard rock ores: A review. Minerals Engineering 131, 170–184. https://doi.org/10.1016/j.mineng.2018.11.023
81. Tischendorf, G., Förster, H.-J., Gottesmann, B., 1999. The correlation between lithium and magnesium in trioctahedral micas: Improved equations for Li2O estimation from MgO data. Mineralogical Magazine 63, 57–74. DOI: 10.1180/002646199548312
82. Tischendorf, G., Gottesmann, B., Förster, H.-J., Trumbull, R.B., 1997. On Li-bearing micas: estimating Li from electron microprobe analyses and an improved diagram for graphical representation. Mineral. mag. 61, 809–834. https://doi.org/10.1180/minmag.1997.061.409.05
83. Tofallis, C., 2015. A better measure of relative prediction accuracy for model selection and model estimation. Journal of the Operational Research Society 66, 1352–1362. https://doi.org/10.1057/jors.2014.103
84. Upadhyay, R.K., Venkatesh, A.S., 2006. Current strategies and future challenges on exploration, beneficiation and value addition of iron ore resources with special emphasis on iron ores from Eastern India. Applied Earth Science 115, 187–195. https://doi.org/10.1179/174327506X138922
85. Villieras, F., Cases, J.M., Francois, M., Michot, L.J., Thomas, F., 1992. Texture and surface energetic heterogeneity of solids from modeling of low pressure gas adsorption isotherms. Langmuir 8, 1789–1795. https://doi.org/10.1021/la00043a018
86. Villieras, Frédéric, Michot, L.J., Bardot, F., Cases, J.M., François, M., Rudziński, W., 1997. An Improved Derivative Isotherm Summation Method To Study Surface Heterogeneity of Clay Minerals. Langmuir 13, 1104–1117. https://doi.org/10.1021/la9510083
87. Villieras, F., Michot, L.J., Bardot, F., Chamerois, M., Eypert-Blaison, C., François, M., Gérard, G., Cases, J.-M., 2002. Surface heterogeneity of minerals. Comptes Rendus Geoscience 334, 597–609. https://doi.org/10.1016/S1631-0713(02)01799-6
88. Villiéras, F., Michot, L.J., Cases, J.M., Berend, I., Bardot, F., François, M., Gérard, G., Yvon, J., 1997. Static and dynamic studies of the energetic surface heterogeneity of clay minerals, in: Studies in Surface Science and Catalysis. Elsevier, pp. 573–623. https://doi.org/10.1016/S0167-2991(97)80074-2
89. Villieras, F., Michot, L.J., Cases, J.M., Berend, I., Bardot, F., Francois, M., Gérard, G., Yvon, J., 1997. Equilibria and Dynamics of Gas Adsorption on Heterogeneous Solid Surfaces, Studies in Surface Science and Catalysis. Elsevier. https://doi.org/10.1016/S0167-2991(97)X8062-0
90. Watts, J.F., Wolstenholme, J., 2019. An Introduction to Surface Analysis by XPS and AES, 1st ed. Wiley. https://doi.org/10.1002/9781119417651

91. Wei, Q., Feng, L., Dong, L., Jiao, F., Qin, wenqing, 2021. Selective co-adsorption mechanism of a new mixed collector on the flotation separation of lepidolite from quartz 9. https://doi.org/10.1016/j.colsurfa.2020.125973
92. Xing, Y., Xu, M., Gui, X., Cao, Y., Babel, B., Rudolph, M., Weber, S., Kappl, M., Butt, H.-J., 2018. The application of atomic force microscopy in mineral flotation. Advances in colloid and interface science 256, 373–392. https://doi.org/10.1016/j.cis.2018.01.004
93. Xu, R., Liu, Y., Sun, N., Kang, J., Sun, W., Tang, H., Wang, L., 2024. The activation role of Mg2+ in the lepidolite flotation using NaOL. Separation and Purification Technology 351, 128035. https://doi.org/10.1016/j.seppur.2024.128035
94. Xue, Z., Feng, Y., Li, H., Ju, J., Du, X., 2024. A stepwise approach to enhancing flotation of low-grade zinnwaldite through the cationic/DL-2-octanol/anionic reagent combinations: Behavior and mechanism analysis. International Journal of Mining Science and Technology 34, 881–891. https://doi.org/10.1016/j.ijmst.2024.04.004

Supplementary data

Zeta potential - theory

This instrument used is based on the microelectrophoresis method for electrophoretic mobility measurements. It is calculated, according to:

$$U = \frac{v}{E} \quad (3)$$

where v the electrophoretic velocity ($m \cdot s^{-1}$) and E the electric field ($V \cdot m^{-1}$). The Smoluchowski equation then allows to convert electrophoretic mobility to zeta potential. This conversion relies on some assumptions, particularly on the fact that the thickness of the electric double layer is smaller than the particle (Smoluchowski, 1918). In this case, the zeta potential is expressed following:

$$\zeta = \frac{\eta\, U}{\varepsilon_0 \varepsilon_r} \quad (4)$$

where η the viscosity of the solution ($kg \cdot m^{-1} \cdot s^{-1}$), U the electrophoretic mobility ($m^2 \cdot V^{-1} \cdot s^{-1}$) and ε_0 ($kg \cdot m \cdot V^{-2} \cdot s^{-2}$) and ε_r the vacuum and relative permittivity of the medium, respectively.

Surface potentiometric titration

2.4.1. Theoretical background – surface charge definition

The charge of mineral surfaces, considered as oxide, results from the ionization of water with surface hydroxide groups. Different ionization states regarding protonation/deprotonation interfacial reactions exist. Naming the surface cation S, these different states can be stated as follows:

$$\equiv S - O^- + H_3O^+ \quad \leftrightarrows \equiv S - OH + H_2O \quad \leftrightarrows \equiv S - OH_2^+ + HO^- \quad (5)$$

The surface groups carry negative, positive, or zero electrostatic charges, depending upon the oxide and the ionic composition of the aqueous phase. They give the surface a basic, acidic, or neutral character, respectively. For oxides, H^+ and OH^- are considered as the potential determining ions. Therefore, the surface charge formation is described using the standard Gibbs free energy,

978 ΔG. This energy is composed of two terms: the chemical part, described by the chemical reactions
979 expressed in Eq. 1, noted ΔG_{chem}, and an electrostatic part, determined by the development of an
980 electrostatic potential at the interface in the process of protonation/deprotonation, noted ΔG_{el}.
981 The surface charge density of oxides formed by proton transfers ($\sigma_{0,H}$) can be defined through the
982 net surface proton excess:

$$\sigma_{0,H} = F(\Gamma_{H^+} - \Gamma_{OH^-}) \quad (6)$$

983 where F is the Faraday constant and $(\Gamma_{H^+} - \Gamma_{OH^-})$ is the surface excess amount or Gibbs excess.
984 This latter requires the knowledge of accurate concentrations of H^+ and OH^- over a broad pH
985 range. From the methodology of Szekeres & Tombácz (2012), this results in a two calibration test
986 of the pH probe for the background electrolyte titration test (Szekeres and Tombácz, 2012).
987 Following their method, the net surface proton excess is computed from:

$$(\Gamma_{H^+} - \Gamma_{OH^-}) \times S_{mineral} = \frac{V_{total} \times \left(c_{H^+,OH^-,0} - c_{H^+,OH^-,e}\right)}{m_{mineral}} \quad (7)$$

988 where $S_{mineral}$ is the specific surface area of the mineral, V_{total} is the total volume of the suspension,
989 $c_{H^+,OH^-,0}$ is the actual proton concentration resulting from titrant additions, $c_{H^+,OH^-,e}$ is the actual
990 proton concentration calculated from the proton concentration calibration plots, and $m_{mineral}$ is the
991 mass of mineral added to the suspension. The proton concentrations can be calculated as follows:

$$c_{H^+,OH^-,0} = \frac{c_{H^+,0} \times \sum_i v_{H^+,i} - c_{OH^-,0} \times \sum_i v_{OH^-,i}}{v_0 + \sum_i v_{H^+,i} + \sum_i v_{OH^-,i}}, c_{H^+,OH^-,e} = \frac{10^{-pH}}{S_a} = \frac{10^{-pOH}}{S_b} \quad (8)$$

992 where $c_{H^+,0}$ and $c_{OH^-,0}$ are the concentrations of the acid and base titrants, $v_{H^+,i}$ and $v_{OH^-,i}$ are the
993 volumes of the i^{th} dose of acid and base titrants, and v_0 is the volume of background electrolyte.
994 The slopes, S_a in the acidic side and S_b in the basic side, obtained from the proton concentration
995 calibration plots, represent the actual response of the electrode to proton and hydroxyl
996 concentrations. From these equations, the point of zero charge of the oxide (PZC), considering the
997 considered background electrolyte, is the pH at which the net surface proton excess ($\Gamma_{H^+} -$
998 $\Gamma_{OH^-} = 0$.) is zero.

XRD pattern

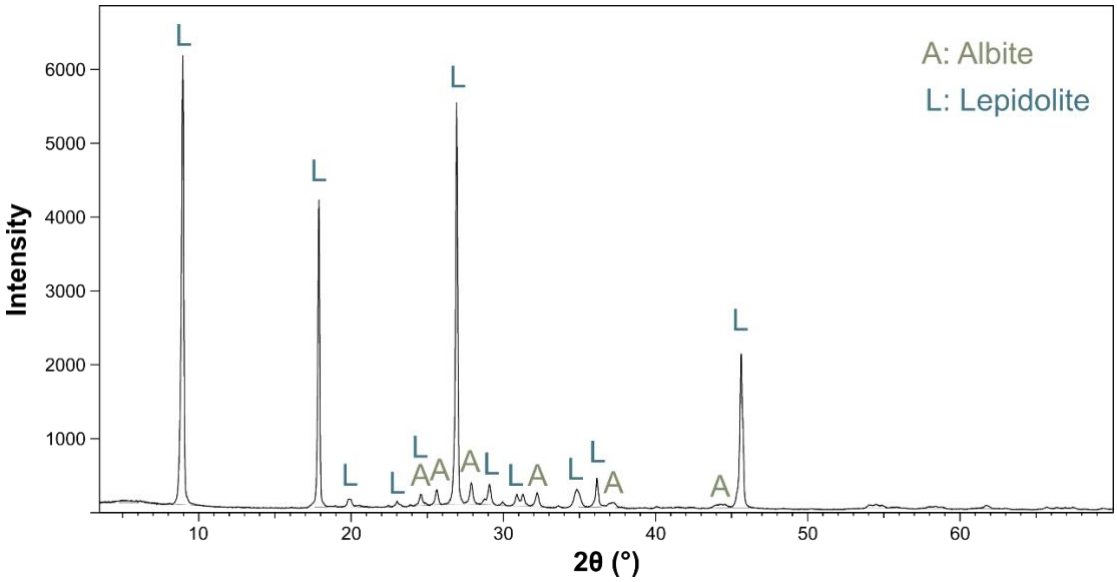

Figure S9 : XRD pattern of the lepidolite sample.

Ionic strength calculations for electrophoretic mobility and potentiometric surface titration experiments.

Table S1 : Ionic strength calculation with consideration of both electrolyte concentration and pH values. Bold values represent the pH ranges where ionic strength is considered almost constant.

pH value	Ionic Strength (M) [KCl] = 1.10^{-3} M	Ionic Strength (M) [KCl] = 1.10^{-2} M	Ionic Strength (M) [KCl] = 1.10^{-1} M
2	0.011	0.020	**0.110**
3	0.002	**0.011**	**0.101**
4	**0.001**	**0.010**	**0.100**
5	**0.001**	**0.010**	**0.100**
6	**0.001**	**0.010**	**0.100**
7	**0.001**	**0.010**	**0.100**
8	**0.001**	**0.010**	**0.100**
9	**0.001**	**0.010**	**0.100**
10	**0.001**	**0.010**	**0.100**
11	0.002	**0.011**	**0.101**
12	0.011	0.020	**0.110**

Proton concentration calibration curve

Strong acid/strong base potentiometric calibrations have been carried out in KNO_3 background electrolyte. The calibration plot with the KNO_3 concentration of 1 x 10^{-1} mol·L^{-1} (Figure S2) was used for both the TDIS experiments and the PZC determination. The other calibration curves were established for PZC titration with background electrolyte concentration of 1 x 10^{-2} mol·L^{-1} and 3 x 10^{-2} mol·L^{-1}, respectively.

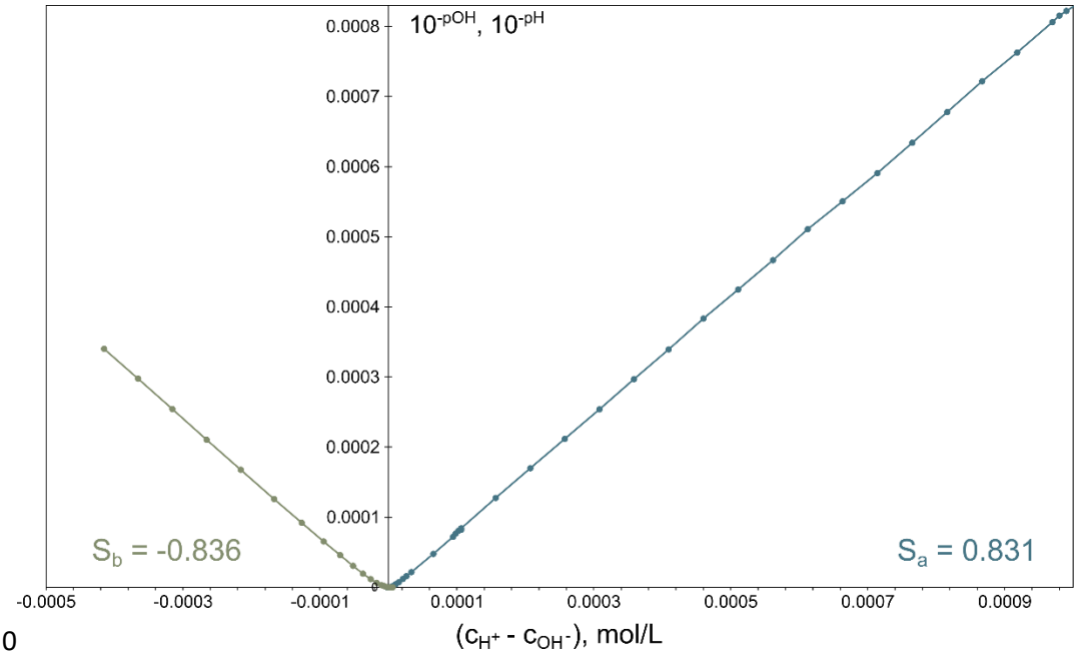

Figure S2: Proton concentration calibration plot in KNO_3 background electrolyte of concentration 1.10^{-1} M.

According to Figure S2, the proton concentration calibration curve displays a classic trend for a potassium-based electrolyte. The acidic and basic parts of the curve exhibit similar slopes (S_a and S_b, respectively) and both cross 0 without any significant drift. Those two points are of uttermost importance since the potential probe was chosen (i) to limit diffusion of KCl into the sample and (ii) to be resistant to silicate suspensions, which are known to be abrasive. In that way, a precise and reliable measurement of proton concentration was obtained. This calibration plot was used (i) to measure the accurate concentration of both acid and base titrant and (ii) to assess the proper operation of the potential probe.

Effect of initial equilibration time

The equilibration time of the suspension has two significant effects, presented in Figure S3. First, it impacts the net proton consumption and, thus, the surface charge values. When the equilibration of the suspension is achieved before the titration, the starting NPC is of about 3.5×10^{-3} mol·g^{-1}, whereas it is of about 0.5×10^{-3} mol·g^{-1} when the titration is directly started without prior equilibration (Figure S3). Opposite trends were observed by Chatman and co-workers for hematite, who reported a decreased NPC when the equilibration time of the suspension increased (Chatman et al., 2013). The second effect of equilibration time is the shape of the titration curve and, therefore, the possible changes for the derivative of experimental data. Although the global shape of the titration curves with and without prior equilibration is the same, with a closer look to the first acquired points, differences can be observed. While the equilibrated suspension presents a proton consumption always decreasing, the unequilibrated curve displays first an increase in the surface charge followed by a decrease. This means that, since the surface sites are not equilibrated, protons are consumed faster than hydroxide ions are added to the solution, which results in an increase of the pH. This is in agreement with the work of Chatman and co-workers, who also noticed changes in the shape of the titration curve according to the equilibration time of the hematite suspension (Chatman et al., 2013). On overall, this highlights the importance of equilibrating the suspension before surface titration of oxide minerals.

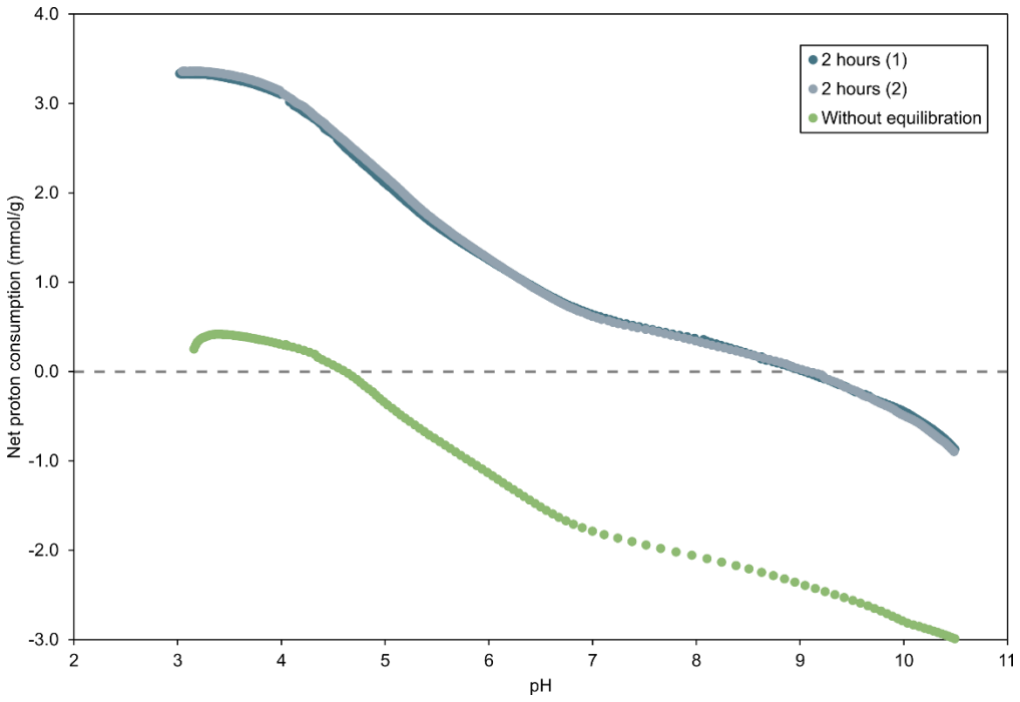

Figure S3: Lepidolite net proton consumption in a 100mM KNO_3 background electrolyte with 2 hours of equilibration time (blue-grey dots) of the suspension and without (green dots).

Acid-base and back base-acid titrations

For method development, some titration experiments conducted from acid to base were followed by a back titration, *i.e.*, by a base to acid titration, as displayed in Figure S4. According to this experiment, the net proton consumption was not equal in the acid-base titration and in the back base-acid titration. Such trends are widely observed in the literature in acid-base titration of minerals (Cabrera, 1979; Szekeres and Tombácz, 2012). These trends can be linked to several phenomena, particularly to the base carbonation during the back titration. Even if painstaking precautions were taken to limit the carbonation of the base, a slight carbonation was observed when the titration was carried out from basic to acidic pH values. Hence, the gap between the two curves observed in Figure S4 can be linked to (i) purity of the mineral and (ii) parasite reaction that are not reversible. These phenomena were highlighted by Szekeres and Tombàcz, who highlighted the effect of acid treatment in the titration of metallic oxides (Szekeres and Tombácz, 2012).

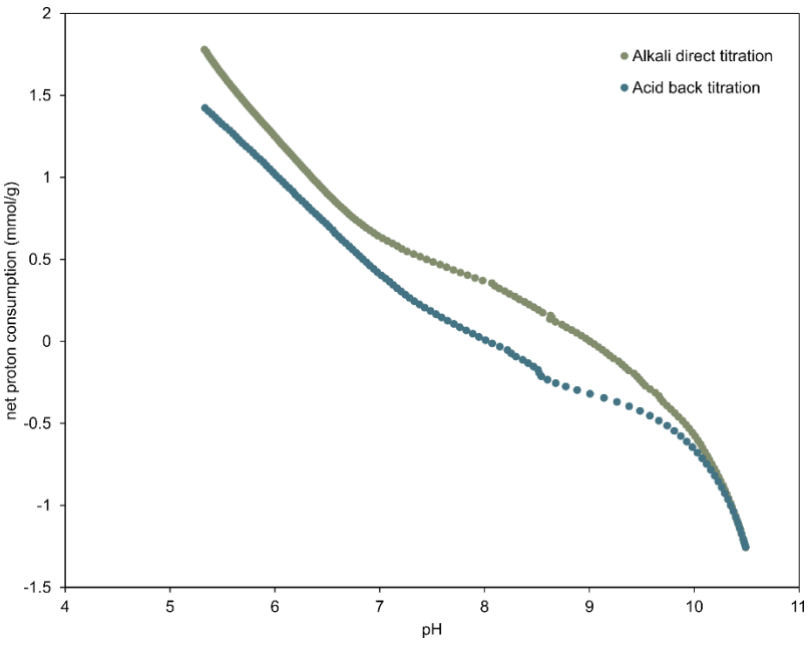

Figure S4: Direct and back acid-base and base-acid titration of lepidolite.

Comparison of deconvolution methods

The method employed in this study is compared with the classic TDIS method on a known sample: goethite used in the publication of B. Prelot and co-authors (Prélot et al., 2002). The comparison of the PEST optimization software to minimize the errors between experimental data and the fitted curve (sum of all local theoretical isotherms) and the TDIS method developed B. Prelot is given in Figure S5 and Table S2.

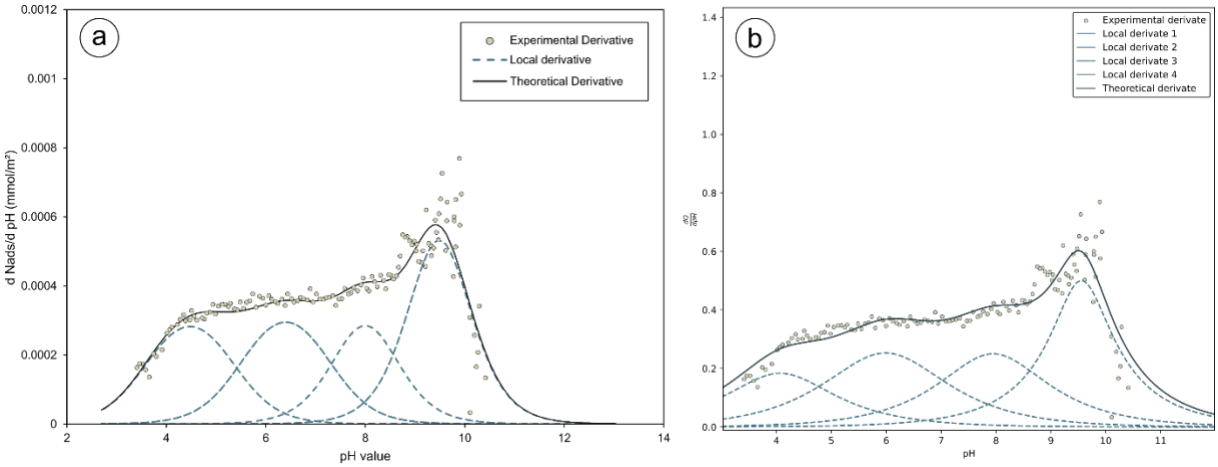

Figure S5: Comparison of the TDIS deconvolution method, the one developed in 2002 (a) and the one developed in this study (b) on the goethite sample used in (Prelot et al., 2002).

From both this table and figure, good agreements are obtained for (i) the number and type of isotherms used, (ii) the shape of local isotherm and theoretical derivative and (iii) the position of the isotherms. The difference of peak positions is ranging between 0 to 0.4 pH values, which is in the order of magnitude of the error of acquisition. Thus, strong agreement are obtained using both methods. Nevertheless, the use of PEST software is robust and time saving.

Table S2 : Comparison of the first TDIS approach and the method used in this study for the goethite sample. Peak position in pH values of the four theoretical isotherms used to predict the experimental derivative using the TDIS approach.

Method	Peak position pH domain 1	Peak position pH domain 2	Peak position pH domain 3	Peak position pH domain 4
TDIS (Prelot et al., 2002)	4.5	6.2	8.0	9.5
TDIS – this study	4.1	6.0	8.0	9.6